Syracuse University

SURFACE

Dissertations - ALL SURFACE

May 2019

Viscoelastic Strain, Viscous Rheology, and Behavior of Experimental Lava Flows

James Farrell
Syracuse University

Follow this and additional works at: https://surface.syr.edu/etd

Part of the Physical Sciences and Mathematics Commons

Recommended Citation

Farrell, James, "Viscoelastic Strain, Viscous Rheology, and Behavior of Experimental Lava Flows" (2019). *Dissertations - ALL*. 1000.
https://surface.syr.edu/etd/1000

This Dissertation is brought to you for free and open access by the SURFACE at SURFACE. It has been accepted for inclusion in Dissertations - ALL by an authorized administrator of SURFACE. For more information, please contact surface@syr.edu.

Abstract

Basaltic pāhoehoe lava flows are prevalent throughout the terrestrial bodies of the solar system. This style of volcanism represents both a predominant resurfacing mechanism of planets and natural satellites and a natural hazard to populations living within volcanically active regions on Earth. Pāhoehoe lava flows are also thought to be integral components of flood basalt provinces, which are the largest known lava accumulations by volume and are suggested to be responsible for several mass extinction events throughout Earth's history. Thus, understanding the dynamics of basaltic lava flows has wide-ranging implications across many fields of geology.

The body of research surrounding the dynamics and rheology of basaltic lava flows spans many orders of magnitude in scale of focus. Large-scale studies of natural lava flows rely on remote sensing techniques to collect data and draw conclusions on behavioral or mechanical phenomena across entire flow fields (tens of kilometers). On the other side of the spectrum, studies of the fine-scale behavior of lava have also augmented our understanding of basaltic flow properties from the perspective of sub-centimeter melt experiments. There remains a substantial gap, however, between these two end-members; studies of basaltic lava flows at the meter-scale are nearly non-existent in comparison. This gap is especially noticeable for pāhoehoe lava flows, which are known to advance and evolve as a function of complex mechanical interactions at the mesoscale (decimeters to meters).

The studies presented here bridge this gap with new research focusing on the emplacement mechanisms, behavior, and rheology of meter-scale pāhoehoe lava flows generated at the world's first lava flow laboratory, the Syracuse University Lava Project

(http://lavaproject.syr.edu). This laboratory is equipped with a high-volume gas-fired tilt furnace capable of melting batches of basaltic rock to super liquidus temperatures (> 1300° C). The resultant melts form glassy pāhoehoe lava flows which are of similar volumetric scale to natural pāhoehoe lava lobes. Like natural lava, a variety of morphologies can be generated such as sheet flows, lobate flows, and channelized flows. The proximity and safety of the laboratory environment allows for direct observation and measurement of critical emplacement parameters such as velocity, thickness, temperature, and rates of effusion. Producing and analyzing data such as these on actively flowing lava has permitted unprecedented research into the rheology and behavior of pāhoehoe lava flows.

One of the themes of the research presented here is understanding the complex relationships between the morphology of a lava flow (the shape of its outer surface) in the context of its inherent physical properties, such as chemical composition and rheology. Models that relate morphology to fluid properties are of critical importance to research in natural lava flows. Often times, especially in the case of planetary geology, the only evidence of active flow conditions is the finite morphology of a flow. Thus, all inferred properties of such lava flows are commonly based solely on morphologic observations. Many studies have addressed the complexities of lava morphology with analyses of cooled lava flows, wax analog flows (polyethylene glycol), and numerical simulations. Experimental lava research, however, allows for the observation of lava morphologies as they form in real-time and correlating those morphologies to direct quantitative measurements.

The first chapter of this dissertation focuses on the relationship between finite morphology and lava flow composition. One of the most recognizable morphologies of basaltic lava flows is known as *ropy pāhoehoe*. The texture associated with ropy pāhoehoe comprises arcuate, repetitive fold patterns expressed at a variety of scales across a lava surface. Folding of a lava flow surface involves buckling of the viscoelastic crust layer into parallel fold trains and subsequent along-axis stretching of resultant folds. These fold trains typically comprise pairings of antiforms and pinched synforms with axial planes normal to the flow direction. The wavelength and amplitudes of these features is on the order of 1 – 2 cm. This pattern of strain is not restricted to ropy pāhoehoe and can be seen across the compositional spectrum of lavas. Other types of gravity flows, such as glaciers and nappes, also express similar strain patterns. In lava flows, the geometry of folds along a lava crust, specifically fold wavelengths, contains information about the rheology and composition of the flow. The study presented in chapter one includes analyses of fold wavelengths along basaltic lava flow surfaces and incremental strain analysis of experimental lava flows. The results show that a relationship exists between lava flow composition and fold wavelengths, regardless of complex strain history. Thus, using only morphologic observations, lava flow composition can be approximated for folded lavas. This correlation will be of value to fields such as planetary and seafloor geology, where remote observations are commonly used to characterize lava flows.

The second chapter of this dissertation focuses on the rheology of experimental lava flows. More specifically, the viscosity of lava during active flow. Viscosity is a physical property dependent on composition, temperature, and entrainment of flow

particles such as bubbles and crystals. All of these properties are constantly changing throughout a flow, thus, as a lava flow evolves, viscosity can change by orders of magnitude through space and time. Therefore, it is one of the most challenging parameters to constrain. Because of this, it has become common practice in volcanology to reduce viscosity to a single value or range, averaging an immense field of complexities. Addressing this problem in the laboratory reduces the inherent challenges associated with traditional volcanologic field work. Presented in chapter two are the first high-resolution spatial and temporal analyses of viscosity for an active lava flow. This revealed the complex evolution of rheology for a lava flow through time with a spatial resolution of 1 cm^2. Also revealed in this study is the rheological framework for a transition between sheet flow and channelized flow behavior. This has implications for better understanding channels as a lava transport mechanism.

The third and final chapter of this dissertation focuses on the behavior of lava lobes, the building blocks of pāhoehoe flow fields. Although lobe evolution is critical for the emplacement of pāhoehoe lavas, relatively few studies have addressed mechanisms related to lobe emplacement. Chapter three focuses specifically on lobes exhibiting a sequence of behaviors known as inflation and breakout. Lava inflation involves the overall thickening of a lobe, by either core pressure changes or crustal accretion. Breakouts occur when internal pressures exceed the yield strength of a lava crust, leading to the development of a subsequent lobe. To better understand this process, seven experimental lava lobes were analyzed, revealing high-resolution morphologic and thermal evolution of lobes during inflation and breakout phases. These analyses revealed a consistent pattern wherein the morphologic and thermal properties

seem to predict the location of a lava breakout. More specifically, areas of high internal fluid pressure (revealed through thickness analysis) and/or zones of weak exterior crust (revealed through surface temperature analysis) coincide with locations of new lava breakouts. Thus, given sufficient observations of lava thickness and surface temperature patterns during lobe inflation, the location of lava breakouts are predictable. However, the development of these patterns, specifically thermal anomalies representing weak zones of crust, is complex. The results showed that although breakouts are predictable, the series of events leading to breakout represent a complex balance between deterministic and stochastic parameters. These observations may help inform future numerical models of pāhoehoe flow development.

In parallel to these research contributions, an additional goal was to develop new techniques for analyzing the temporal- and spatial-dependent properties of single- and multi-phase lavas flowing on inclined planes. Because lava flows evolve at rapid rates and at excessive temperatures (≥1000° C), there are significant challenges to measuring active flow properties both in the laboratory and in the field. I have addressed this problem with integrated 3D and 4D multispectral imaging techniques that allow for generating high-resolution morphometric and thermal datasets with low uncertainties (described in detail in chapter two). These datasets have been utilized in this dissertation to calculate inherent fluid properties of lava (e.g. viscosity) but can also be used in an array of subsequent investigations in basaltic lava flow dynamics. Such future work could address questions related to non-Newtonian behavior of lava, effects of bulk compositional changes (e.g. SiO_2, K_2O + Na_2O) on rheology, and additional quantitative analyses of morphology.

Experimental lava research represents a significant advance in the field of volcanology, but there are still challenges to overcome. Laboratory lava flows, although similar in scale to natural pāhoehoe lobes, are comprised of pure glass and lack any measurable crystallinity (with few exceptions). Natural lava flows are rarely crystal-free, thus, direct comparisons to experimental lavas are not yet entirely comprehensive. Additionally, the temperature range of experimental lava is much higher than natural flows, with starting temperatures well above 1200° C. Natural basalts erupt and flow at temperatures close to or below 1100° C, thus critical parameters such as cooling rate and viscosity are inherently different than experimental lavas. Overcoming these challenges in the laboratory would require only small adjustments to the current experimental practice, such as reducing starting temperatures. Future advances in this field will undoubtably lead to the generation of flows closer to natural conditions.

The research presented here focuses on addressing a few specific problems related to the emplacement of experimental pāhoehoe lava flows. But more importantly, this work represents advances in a truly nascent field of study. Only a handful of investigations have been conducted so far using experimental lava technology, but the potential and community interest for such research directions is steadily growing. The 2018 eruption of Kilauea marked the end of a 35-year period of daily active lava flows in Hawaii; a significant loss for the volcanological community who relied on this region as a natural laboratory for studies of lava flow dynamics. Because of this, the need for large-scale experimental lava flows will continue to increase in the coming years and, hopefully, the research presented here will serve as a guide for those seeking to advance this field.

Viscoelastic Strain, Viscous Rheology, and Behavior of Experimental Lava Flows

By

James Arnold Farrell

B.S. Geology, Stony Brook University, 2012

M.S. Geosciences, University of Connecticut, 2015

DISSERTATION

Submitted in partial fulfillment of the requirements for the degree of Doctor of Philosophy in Earth Sciences

Syracuse University

May 2019

Copyright © James A. Farrell 2019

All rights reserved

Table of Contents

General Abstract i

Title Page vii

List of Figures xii

List of Tables xv

Chapter 1: Multiple-generation folding and non-coaxial strain of lava crusts 1

Abstract 2

Introduction 3

Background 5

Methods 9

Experimental lava flows 10

Natural lava flows 11

Photogrammetric digital terrain models 12

Viscosity modelling 13

Fourier analysis 16

Results 17

Syracuse lava 17

Myvatn Lava 18

La Réunion Lava 19

Discussion 19

Validity of the plane strain assumption 19

Factors affecting finite fold wavelength 21

Multiple-generation folding 23

Conclusions 25

Tables 27

Figures 29

Chapter 2: Mapping the 4-dimensional viscosity field of an experimental lava flow 42

Abstract 43

Introduction 44

History of viscometry 45

Methods 48

Experimental lava flow 48

Time-lapse photogrammetry 50

Velocimetry 52

Thermal infrared imaging 53

Viscosity mapping 53

Results 56

Velocity, thickness, and surface temperature 56

Jeffreys' equation results 57

GRD results 57

Discussion 58

Spatial viscosity patterns 59

Solving for layered rheology 60

Field applications 62

Conclusions 63

Tables 64

Figures 65

Chapter 3: Predicting the locations of breakouts in basaltic lava flow experiments 73

Abstract 74

Introduction 75

Methods 76

Results 79

Discussion 79

Stochastic influences on thermal anomalies 80

Implications for breakout mode 81

Conclusions 82

Tables 84

Figures 85

References 89

Biographical data 103

List of figures

Chapter 1

Figure 1. Oblique view of experimental lava lobe with a single generation of horizontal axis folds and schematic cross sections 29

Figure 2. Simplified diagram representing two different fold geometries observed in lava flows 30

Figure 3. Simplified sketch of multiple-generation horizontal-axis folding..... 31

Figure 4. Examples of lava flows from a Myvatn, Iceland (basalt), b La Réunion Island (basalt), and c Syracuse University Lava Project (basaltic andesite) 32

Figure 5. High-volume, gas-fired tilt furnace used for melting batches of basaltic- to basaltic-andesite lava at the Syracuse University Lava Project 33

Figure 6. Workflow methodology for extracting topographic profiles across lava flows 34

Figure 7. Workflow for extracting dominant wavelength patterns along a folded lava surface . 35

Figure 8. Average wavelength picks for experimental and natural lava flows 36

Figure 9. Wavelength ratios for multiple-generation horizontal-axis folds among different types of lavas plotted against SiO2 content 37

Figure 10. Apparent viscosity model results of lava flows 38

Figure 11. Kinematic video analysis of a Syracuse lava flow with areas indicated by the white boxes enlarged on the right 39

Figure 12. Flow Syracuse 7, frontal toe used for wavelength analysis 40

Figure 13. Example of crustal folding and subsequent erasure of folds 41

Chapter 2

Figure 1. Time-lapse imagery of the experimental basaltic lava flow used in this study 65

Figure 2. Schematic rheologic cross section of a lava flow 66

Figure 3. Data collection apparatus used during lava flow experiments 67

Figure 4. Oblique view of digital raster data for the experimental lava flow at time step t = 73 seconds 68

Figure 5. Viscosity-temperature curve for the experimental lava flow 69

Figure 6. Time-lapse apparent viscosity maps and histograms of the experimental lava flow calculated using the Jeffreys (1925) equation 70

Figure 7. Time-lapse crustal viscosity maps and histograms of the experimental lava flow calculated using the GRD model 71

Figure 8. Mean values of lava viscosity over time calculated using the described models 72

Chapter 3

Figure 1. Experimental lava flow 180721-2 displayed as raster datasets draped over a photogrammetric 3D surface 85

Figure 2. Predicted and observed lava flow breakout azimuths for experimental lava flow 180721-1 86

Figure 3. Rose diagram of angular misfits between predicted and observed lava flow breakout azimuths based on thickness (N = 7) and temperature (N = 5) analyses 87

Figure 4. Time lapse oblique photographs of experimental lava lobe undergoing inflation and breakout 88

List of tables

Chapter 1

Table 1. Normalized major element compositions in wt.% for lavas analyzed in this study..... 27

Table 2. Wavelength analysis results for the 16 lava flows analyzed in this study 27

Table 3. Physical parameters and apparent viscosities calculated for Syracuse lava flows using DTMs and video analysis. 28

Chapter 2

Table 1. Normalized major element compositions in weight percent for the experimental lava used in this study. 64

Table 2. Results from the described viscosity modelling workflow 64

Chapter 3

Table 1. Table 1. Results of breakout direction prediction analysis. All values are in degrees (°) 84

Chapter 1: Multiple-generation folding and non-coaxial strain of lava crusts

Published As:

Farrell, J., Karson, J., Soldati, A., & Wysocki, R. (2018). Multiple-generation folding and non-coaxial strain of lava crusts. *Bulletin of Volcanology*, *80*(12), 84. doi:10.1007/s00445-018-1258-5

Abstract

Viscoelastic strain in lava flows is commonly expressed as gravity-driven buckling of the lava crust. This surface folding process creates the well-known ropy pāhoehoe texture of basaltic lavas and the ogives and surface ridges of more compositionally evolved lava flows. Previous work has shown that surface fold wavelengths are proportional to the viscosity contrast between the lava crust and core, and to the thickness of the crust. Thus, fold analysis can be an important tool for understanding lava flow rheology. We analyze fold wavelength patterns of solidified natural lava flows from the Myvatn lava fields (Iceland), Piton de La Fournaise (La Réunion), and experimental lava flows from the Syracuse University Lava Project. In each case, lava flows exhibited two dominant wavelengths, consistent with multiple-generations of coaxial folding. The ratio of the two dominant wavelengths for basalt (Iceland, La Réunion) is ~5:1 whereas the wavelength ratio for basaltic andesite (Syracuse) is ~3:1, suggesting a compositional control on deformation, as proposed by previous studies.

Video analysis of incrementally folded Syracuse lava crusts reveals significant non-coaxial strain, which violates the assumptions of plane-strain used in crustal buckling models. These results show that interpreting lava rheology from finite strain requires careful consideration of complex three-dimensional strain fields. Despite these complexities, the correlation between fold wavelength ratios and lava flow composition persists and may provide important insight into flow characterization.

Introduction

Folding of lava flow surfaces has been studied across a compositional range including basalt (Cashman et al. 2013; Favalli et al. 2018; Fink and Fletcher 1978; Gregg et al. 1998; Iezzi and Ventura 2000; Macdonald 1953), andesite (Gregg et al. 1998; Warner and Gregg 2003), dacite (Gregg et al. 1998; Lescinsky et al. 2007; Pyle and Elliott 2006), and rhyolite (Castro and Cashman 1999; Farquharson et al. 2015; Fink 1980; Magnall et al. 2017). Even some extra-terrestrial lava flows with similar topographic expressions (i.e. surface ridges) have been interpreted to form via surface folding (Gregg et al. 1998; Theilig and Greeley 1986; Warner and Gregg 2003). This fold geometry is similar to that of other types of gravity flows such as glaciers and nappes in orogenic belts (Merle 1989, 1998). Surficial deformation of lava analog materials including viscous and multiphase fluids has also inspired experimental studies of fold morphology (e.g. Gregg and Fink 1995; Lescinsky and Merle 2005; Applegarth et al. 2010). Studies related to the geometry and kinematics of folding on lava flow surfaces, and the rheology of the lava crust, show a distinct relationship between fold geometries and physical properties of the lava. Previous authors have modeled flows as a simple two-layer system in which the crust is treated as a viscoelastic material coupled to a viscous core of molten lava (Fink and Fletcher 1978) (Figure 1).

Horizontal-axis surface folds on lavas are interpreted to form in response to buckling of the lava crust during flow (Fink 1980; Fink and Fletcher 1978). Buckling is defined as folding of a planar element caused by instabilities during layer-parallel shortening, with no significant mechanical thickening of the plane (Biot 1961); although in the case of lava crusts, the plane (crust) thickens as it cools. In a lava flow, the initial

crust is a planar, viscoelastic layer. As the flow moves downslope it cools, and viscosity increases, causing resistance to flow advance, imposing a surface velocity gradient. This velocity gradient (higher velocity near source and lower velocity near flow front) results in layer-parallel shortening and buckling of the viscoelastic lava crust, creating horizontal-axis folds (Biot 1961; Fink and Fletcher 1978). Horizontal-axis surface folds in lava formed by buckling take the form of concentric, non-cylindrical antiforms and tight, angular synforms with hinge lines initially normal to the flow direction and axial planes dipping steeply away from the flow direction (Figure 1). These folds are commonly overprinted by larger-wavelength coaxial folds, formed due to crustal thickness changes, resulting in multiple-generation folding (Fink and Fletcher 1978; Gregg et al. 1998). The ratio of large-to-small wavelengths for these multiple-generation folds are a reflection of the relative strain and cooling rates of a flowing lava and therefore may be related to emplacement conditions, rheology, and lava composition (Gregg and Fink 1995; Gregg et al. 1998). Coeval with layer buckling, fold hinge lines are stretched and rotated into near-parallelism with the flow direction, creating levees bounding the center of the flow (e.g. Odonne and Vialon 1983; Ridley and Casey 1989; Lescinsky and Merle 2005). This deformational pattern results in vertical-axis folds and creates the recognizable, arcuate, and concentric “ropes” of a folded flow surface (Figure 2).

In this study, we collected morphologic and kinematic lava flow data for spectral analysis of horizontal-axis surface folds to define dominant wavelength patterns and to assess the nature of non-coaxial strain during the formation of vertical-axis folds. For comparison with previous studies, we reported the ratio of dominant wavelengths for horizontal axis folds. Additionally, we quantified the apparent viscosity of experimental

lavas using an array of analytical models. We used natural examples from the Myvatn lava field in Iceland and Piton de la Fournaise in La Réunion (basalts) for finite strain and rheological comparisons to experimental lavas (basaltic andesites). This approach permits a quantitative comparison of fold geometry, related physical properties, and rheology of selected experimental and natural basaltic and basaltic andesite lava flows. Our results show that wavelength ratios strongly correlate to lava composition and rheology, consistent with previous studies, despite significant non-coaxial strain revealed in the kinematic analysis of experimental lavas.

Background

Studies of viscoelastic deformation in geologic materials, including lava flows, have foundations in theory presented by Biot (1961), with equations that relate folding of stratified media with various physical parameters. Lava flows can be represented by a two-layer system consisting of a viscous flowing interior core (η_i) and a viscoelastic exterior crust (η_e) (Figure 1). Because the model quantifies viscous and viscoelastic rheology, the deformation related to the brittle crust is not considered. In this representation, a dominant fold wavelength (λ) will develop that is a function of the thickness of the crust (h) and the viscosity contrast between the crust (η_e) and core (η_i) (Biot 1961; Castro and Cashman 1999):

$$\frac{\eta_e}{\eta_i} = 0.024\left(\frac{\lambda}{\mathrm{h}}\right)^3 \qquad (1)$$

This relationship implies that some rheological properties of lava flows can be inferred from the geometry of folds on lava flow surfaces. An important assumption is that strain is only accumulating in two directions (plane strain) and that strain can be accurately assessed from two-dimensional, vertical, cross sections parallel to the flow direction (Biot 1961; Castro and Cashman 1999; Fink and Fletcher 1978). Observations of active folding in experimental and analog lava flows, however, challenge the assumption of plane strain deformation (Applegarth et al. 2010; Gregg and Fink 1995; Lescinsky and Merle 2005).

Folding theory was first applied to lava flows in a study of Hawaiian ropy pāhoehoe lava (Fink and Fletcher 1978). To quantify waveforms along cooled lava flows, topography was profiled by hand-tracing the folded surface using a contour-tracing stylus. This method created two-dimensional profiles of horizontal-axis folds and showed reasonable agreement with theory as it related to folding of viscoelastic media. Fink and Fletcher (1978) also showed that horizontal-axis folds on a lava crust can be interpreted in terms of multiple episodes of coaxial folding, otherwise known as multiple-generation folding, resulting from a superposition of generations of folds with different dominant wavelengths. On an active flow surface, the viscoelastic crust will buckle and form a first-generation of folds with a characteristic wavelength. Continued coaxial shortening of the crust can lead to the formation of larger, superimposed folds with a longer dominant wavelength (Figure 3).

A subsequent investigation measured the horizontal-axis folds of 40 different lava flows to test a hypothesis that relates surface fold geometry to lava composition and emplacement conditions (Gregg et al. 1998). Using photographs and field mapping,

Gregg et al. (1998) measured waveforms along cooled flow surfaces and separated them into distinct generations, each characterized by a dominant wavelength. The results demonstrated that there is a correlation between lava composition and second-to-first-generation fold wavelength ratios (Gregg et al. 1998). Specifically, basaltic flows have a distinctly higher (~5:1) ratio of second-to-first-generation fold wavelengths than those of more silicic lavas (< 3:1). An important implication of this study is that wavelength ratios are controlled not simply by composition, but also by the relative strain and cooling rates. Second-generation folds appear at a critical crustal thickness, thus lavas with low strain rates (relative to cooling rates) will reach the critical thickness under less strain. Folds on a relatively slowly deforming crust therefore experience less shortening per generation, due to rapid transition from viscoelastic to brittle phase, and thus, a lower wavelength ratio will develop (Figure 3). Basalts do have high cooling rates, but even higher strain rates, in comparison to more evolved lavas (e.g. Webb and Dingwell 1990; Harris et al. 2005; Harris et al. 2007); thus, relative to cooling rates, basalt has much higher strain rate than slow-moving silicic flows, leading to more shortening per generation and higher wavelength ratios (Fink 1980; Gregg et al. 1998; Harris et al. 2004). The results of Gregg et al. (1998) are consistent with analog experiments in polyethylene glycol flows that showed second-to-first generation fold wavelength ratios remain consistent regardless of emplacement conditions (Gregg and Fink 1995).

Following the findings of Gregg et al. (1998), subsequent studies reported wavelength ratios of multiple-generation folds described on silicic flow surfaces. Using LiDAR (light detection and ranging) DTMs (digital terrain models) and Fourier analysis,

Pyle and Elliot (2006) found wavelength ratios between 1.3 and 2.1:1 along a folded dacite flow in Santorini, Greece. A similar study by Lescinsky et al. (2007) found second-to-first generation wavelength ratios between 1.5 and 2.3:1 across the Medicine Lake dacite flow in California using total station surveys and Fourier analysis. Both are consistent with the Gregg et al. (1998) findings that suggest more evolved lava compositions tend to exhibit lower wavelength ratios.

Previous work has produced significant observations and analysis of surface folding morphology related to cooled natural lava flows and experimental analog materials. The aim of this study is to build upon previous work by integrating observations of large-scale experimental lava flows and comparing to similar natural examples. To achieve this, we quantified horizontal-axis fold wavelengths in two-dimensions and compared them to known lava compositions for both natural and experimental lavas. Additionally, results from experimental lavas were qualified in the context of incremental strain in three-dimensions. Incremental strain observations are crucial for evaluating the assumption of plane-strain in lava folding, which is a fundamental assumption for rheologic interpretations using the Biot (1961) model (Equation 1). Furthermore, wavelength ratio analysis broadens the field of existing empirical evidence linking lava composition and rheology to surface fold wavelength ratios, which appear to be independent of the plane strain assumption. Lastly, we used high-resolution 3D models to evaluate and compare existing analytical rheology models, such as the previously described Biot (1961) model. These results can be used to build a better understanding of active flow rheology to refine interpretations made in the field on flows after emplacement.

Methods

Fold geometry is related to flow rheology, which in turn is mainly a function of composition, crystallinity, vesicularity, and temperature (e.g. Fink and Fletcher, 1978; Fink 1980; Gregg et al., 1998). Because rheology can evolve during flow, it is important to consider both finite and incremental strain of lava crusts. This is especially appropriate for wavelength analysis because models relating fold geometry to lava rheology are used assuming plane strain deformation (Biot 1961; Castro and Cashman 1999; Fink and Fletcher 1978; Fletcher 1974). We implemented a method for fold analysis based on high-resolution (sub-millimeter) 3D photogrammetric DTMs (digital terrain models) and Fourier transform of flow topography. These analyses were performed on experimental lavas at the Syracuse University Lava Project in Syracuse, New York (lavaproject.syr.edu) in addition to natural, cooled lava flows from Myvatn, Iceland and Piton de La Fournaise, La Réunion (Figure 4).

DTMs are powerful tools for studying a range of morphological parameters and are widely used in physical volcanology (Cashman et al. 2013; Dietterich et al. 2015; Farquharson et al. 2015; Favalli et al. 2018; Hamilton et al. 2013; James and Varley 2012; James et al. 2007; Kolzenburg et al. 2018; Pyle and Elliott 2006; Westoby et al. 2012). In addition to topographic analysis, six experimental flows were chosen for video analysis. Video analysis allows for quantification of surficial strain rates, and has been used previously to analyze velocity fields and aid in approximating apparent viscosities of experimental and natural flows (James et al. 2012; James et al. 2007; Lev et al. 2012; Sakimoto and Gregg 2001). The integration of 3D terrain and video analysis also enables modelling of apparent lava viscosity using analytical models.

Experimental Lava Flows

Experimental lava flows were generated by melting up to 375 kg of 1.1 Ga basaltic rock from the Mid-Continent Rift (Wirth et al. 1997), in a gas-fired tilt furnace at about 1400°C (Figure 5). Lava flows generated using this material are typically pure glass and yield compositions in the basaltic andesite range (Table 1). Typical eruption temperatures (when the lava reaches the substrate) ranged between 1290°C and 1390°C for flows used in this study, based on thermal imaging with a handheld forward-looking infrared camera (FLIR). Geochemical analyses (wavelength-dispersive spectroscopy) performed at the Electron Microprobe Laboratory at Syracuse University showed typical SiO_2 content of past experimental flows was 54±1 wt% (Table 1, Online Resource 1). This is the composition we used to represent the experimental lavas, although the specific flows used in this study were not analyzed for geochemistry, with the exception of flow Syracuse 1 (Table 1, Syracuse Alkali).

The facilities at the Syracuse University Lava Project have been used to simulate an array of behaviors and conditions including lava-ice interactions (Edwards et al. 2013), channelized and sheet flow rheology (Lev et al. 2012), the effectiveness of barriers for lava diversion (Dietterich et al. 2015), and the effect of topographic roughness on lava emplacement (Rumpf et al. 2018). Lava flows analyzed in this study were chosen based on the presence of well-developed surface folds and relatively simple sheet or lobate forms. Of 15 total experiments, eight lava flows exhibited this morphology and were used for comparison to natural flows. The Syracuse Lava facility generates flows 1-2 m long and as much as 1 m wide, with variable thicknesses on the order of centimeters to decimeters. This scale is similar to individual toes and lobes of

natural flows used in this study (Figure 4). Each flow studied exhibits a similar ropy morphology with arcuate vertical-axis fold patterns and levees. Flows generated at Syracuse are glassy with no detectable crystal textures. Flows with high vesicularity, as determined by direct examination of hand samples, were excluded from this study to reduce rheological complexity.

The benefit of using laboratory-derived lava flows is that they allow for direct data collection during emplacement. Video data, for example, provide detailed documentation on the evolution of the crust as well as indirect measurements of some physical properties of the molten lava (Lev et al. 2012). In this study, we used video data to measure maximum velocities and to approximate coaxial stretching as a first-order view of the validity of the plane-strain assumption. Video-based particle tracking, performed in the freeware Kinovea, allowed for the extraction of these kinematic data. Unlike data from solidified flows in the field, this method provides insight into the incremental strain history of the lava crust that can be compared to the total finite strain from the final form of the folded crust.

Natural Lava Flows

Basaltic lava flows from Iceland and La Réunion Island were selected for comparison to the experimental lava flows produced experimentally (Table 1; Figure 4). These flows exhibit well-preserved and well-exposed ropy pāhoehoe lobes with multiple generations of surface folds. Additionally, these flow-fields had not yet been analyzed at the lobe scale using 3D morphometry, allowing for additional comparison to previous work on surface folding of Hawaiian basalts (Fink and Fletcher 1978; Gregg et al. 1998).

The Icelandic lavas are from the Myvatn Fires lava field in northeastern Iceland. The Myvatn Fires field, which erupted between 1724 and 1729, began in the Krafla volcanic system as a fissure eruption and produced 0.45 km^3 of basaltic lava (Gronvold 1984). Whole-rock chemical analyses of basalt from this lava field yielded SiO_2 compositions averaging 50±0.5 wt% (Gronvold 1984).

La Réunion lava examples are from the 2004 lava field of Piton de La Fournaise. The August 2004 pāhoehoe flow field was fed by a fissure on the eastern flank of the volcano which propagated down to an elevation of 1900 m. An extensive system of lava tubes developed (Global Volcanism Program 2004; Staudacher et al., 2008). Whole-rock chemical analyses of basalt from the 2004 lava field have an average SiO_2 content of 49±0.5 wt% (Vlastélic et al. 2007).

Photogrammetric digital terrain models

DTMs of lava flow surfaces were created using the Structure-from-Motion (SfM) photogrammetry method (Westoby et al. 2012) (Figure 6). Each flow was photographed from various angles along an arcuate viewing path in an approximately vertical plane. Images were taken at an average distance of about 1 m and focused on a consistent central point on the flow. Using Agisoft Photoscan®, a commercially available software, JPEG images were aligned and processed to create 3D point clouds of the lava flow surface. Resulting point cloud densities ranged between 2 and 42 million points per flow depending on the size of the flow, quality of images, and reflectivity of the surface. Similar data collection methods were used for both experimental and natural lava flows.

Point clouds were transformed into orthorectified DTMs scaled with ground control points, typically along a scale bar on or next to the flow of interest. In this study, DTMs derived from SfM yielded raster resolutions with a range of 0.1 to 0.5 mm/pixel (Table 2). This resolution ensured sampling rates along topographic profiles were significantly higher frequency than the topographic signal of horizontal-axis folding (centimeter to decimeter), and therefore minimized aliasing (missed signal due to sampling frequency) in the Fourier analysis. Vertical accuracy of each flow was approximated using topographic profiles across known flat surfaces, such as scale bars. The degree to which these digitized profiles deviated from a flat surface was determined using a root-mean-square amplitude calculation, performed in MatLab. Using this method for approximating vertical DTM accuracy, we found a range of 0.1 to 0.3 mm.

Along with topographic profiling, DTMs were used to determine thickness, width, area, and volume of the experimental lavas. For six of the flows, vertical video was available and integrated to determine total emplacement time, which allowed for calculations of mean output rate (time-averaged volume flux) and strain rate.

Viscosity modelling

To bracket apparent viscosities of the Syracuse flows, we applied four different viscosity models. The models were chosen based on availability of measurable parameters derived from this study (e.g. thickness, volume, fold geometry, temperature). In calculating these viscosities, we also tested the validity of the assumption of plane strain deformation associated with crustal buckling (Biot 1961; Castro and Cashman 1999; Fink and Fletcher 1978).

The first model was presented in Fink and Griffiths (1990) as the equation:

$$h = \left(\frac{Q\eta}{\rho g \sin(\theta)}\right)^{1/4} \qquad (2)$$

where h is flow thickness, Q is mean output rate, η is viscosity, and ρ and g are lava density and gravity, respectively. This model assumes unconfined Newtonian flow and significant viscosity contrast between the substance (lava) and the medium (air). We used ρ=2700 kg/m^3 for all experimental lavas, following calculations by Lev et al. (2012) for the same lava. Parameters h and Q are determined for each flow using DTMs and video analysis. We used an average value for h by dividing volume by area, and Q is calculated by dividing volume by the emplacement time.

The second equation used for approximating apparent viscosity is based on surface fold geometry. This was presented in Fink and Fletcher (1978) and is a modified version of the Biot (1961) equation:

$$\dot{\varepsilon}\eta_i > \frac{\rho g A}{0.08R\ lnR} \qquad (3a)$$

In this equation, $\dot{\varepsilon}$ is strain rate, η_i is the interior or core viscosity, A is the amplitude of folds and R is defined as the viscosity ratio η_i:η_o, which can be approximated by:

$$\ln R > 28A/\lambda \qquad (3b)$$

Derivations can be found in Fink and Fletcher (1978). We used the root-mean-square amplitude for each flow profile and reported a high and low viscosity value based on the first and second-generation fold wavelength (λ) for each flow. Strain rate was calculated for each flow by dividing total in-plane strain by emplacement time. Because this equation estimates interior viscosity, it should provide a minimum estimate for apparent viscosity of the whole flow. This equation was initially used in a study of Hawaiian pāhoehoe lavas but has also been applied to lava flows on Mars as a means for

comparison to terrestrial lavas (Fink and Fletcher 1978; Warner and Gregg 2003; Zimbelman 1985). This approach requires an assumption of Newtonian flow and plane strain deformation of the crust. Additionally, the fluid is assumed to be laterally isothermal with an exponential viscosity increase with depth (due to temperature stratification), which is more realistic than a simpler crust-core two-layer model (Fink and Fletcher 1978).

For the final analytical model, we applied Jefferys' equation (Jeffreys 1925) for viscous flow in the form:

$$V_{max} = \rho g h^2 sin\theta / 4\eta \qquad (4)$$

Where V_{max} is the maximum velocity, determined by video analysis, and θ is the slope angle of the substrate. All other variables are the same as previously described. This model assumes Newtonian flow and that flow width is significantly larger than flow thickness. Equation 4 has been applied to Syracuse lava experiments by Lev et al. (2012) and showed good agreement with the non-Arrhenius model presented in Giordano et al. (2008).

Lastly, we calculated temperature-viscosity curves for Syracuse, Syracuse Alkali, Myvatn, and La Reunion lavas using the GRD (Giordano, Russell, and Dingwell) model, executed using the open-source calculator provided in Giordano et al. (2008). Using the normalized major element composition of each lava type (Table 1), we calculated viscosities between 900 and 1400°C for all lavas. For Syracuse lavas with available thermal data, we calculated GRD viscosities based on the maximum temperature. As a means for comparison, we also calculated the GRD viscosity curves for andesite, dacite, and rhyolite using field examples provided in Gregg et al. (1998). The

geochemistry values for select evolved lavas can be found in Murase and McBirney (1973) (Mt. Hood Andesite, Newberry Rhyolite) and Barton and Huijsmans (1986) (Santorini Dacite). As previously discussed, surface fold geometry is dependent on the crust-to-core viscosity contrast, thus these modelled viscosities alone do not provide insight to fold wavelength characterization. However, they do provide a useful comparison of viscosities derived by composition instead of morphology.

Fourier Analysis

Topographic profiles for Fourier analysis were extracted along the known, or inferred, flow direction to capture folds formed by gravity-driven buckling of the lava crust. This process requires profiles far from the levees, where coaxial stretching affects fold wavelengths to the greatest extent. In cases where the flow direction was not observed, profiles were chosen along the points of maximum in-plane curvature (horizontal axial trace) of the folded surface, which has been observed to be parallel to flow direction in active flows (Fink and Fletcher 1978) (Figure 6c). A representative topographic profile contains a continuous, semi-uniform train of folds which can be simplified as sinusoids with definable wavelengths and amplitudes. Because this study aims at isolating a signal related to buckling of the crust, profiles exhibiting obvious, small-scale non-coaxial strain were not analyzed. Features such as plunging folds, locally rotated fold axes, and along-strike splitting of fold hinges introduce complexities that deviate from simple crustal buckling.

Ten parallel topographic profiles were selected for each target surface and prepared for wavelength analysis (Figure 7). The 2D topographic profiles containing

spatial data were transformed into the frequency domain using Welch's power spectral density estimate, executed in MatLab (Welch 1967). The two highest frequency peaks in each transform were then automatically extracted and inverted to determine wavelength trends for each flow. Ten first-generation and ten second-generation wavelengths were picked for each surface, averaged, and reported with a 2σ measure of variability. Wavelengths determined using this method were cross-checked by visual inspection of orthophotographs and DTMs to verify accuracy.

Results

Syracuse Lava

Spectral results from experimental Syracuse lava flows revealed self-similar patterns across all flows (Figure 8, Table 2). Each flow (n=7) was profiled and transformed ten times. The average wavelength for all the sampled first-generation folds was 1.1±0.4 cm. The average wavelength for all the sampled second-generation folds was 3.3±1.0 cm. The second-to-first-generation wavelength ratio for Syracuse lava was 3.0±0.8:1 (Figure 9).

One Syracuse lava experiment (Syracuse 1) was purposely contaminated with additional alkali compounds (Na_2O and K_2O) to simulate a basaltic trachy-andesite. Chemical analysis showed this flow contained >6 wt% total alkalis (Table 1), thus it was treated separately from the other seven experimental flows. The average wavelength for all the sampled first-generation folds across the alkalic lava was 0.8±0.3 cm. The average wavelength for all the sampled second-generation folds across the alkalic lava

was 3.1±0.1 cm. The second-to-first-generation wavelength ratio for this flow was 4.2±1.0:1 (Figure 9).

Physical dimensions of each Syracuse lava flow are reported in Table 3. Average volume for all Syracuse flows was 3.3±1.9 x 10^4 cm^3, average area was 1.0±0.4 m^2, and average thickness was 3±1 cm (based on volume/area ratio).

The range of maximum velocities for the experimental lava flows was between 3 and 9 cm/s based on particle tracking and the range of mean output rate for these flows was 110 to 280 cm^3/s (Table 3). Apparent viscosity calculations using Equations 2, 3b, and 4 can be found in Table 3 and Figure 10. Although a wide range of values was found, an average log apparent viscosity of 1.8 Pa s is consistent with previous studies of Syracuse lava and with GRD model results at a temperature of 1300°C (Giordano et al. 2008; Lev et al. 2012; Sehlke and Whittington 2016).

Myvatn Lava

The average wavelength for all the sampled first-generation folds across Myvatn lava flows (Table 2) was 2.1±0.5 cm. The average wavelength for all the sampled second-generation folds was 10.1±3.6 cm. The second-to-first-generation wavelength ratio for Myvatn lava was 5.3±1.4:1.

Volumetric measurements were not available for the Myvatn data. Many folded surfaces were a part of large, deformed complexes that were often broken into sheets of platy pāhoehoe. The folds also commonly presented on lava channels, instead of morphometrically definable toes and lobes. Lastly, the target surfaces were in a complex compound flow field that erupted intermittently over five years (Gronvold 1984).

It was therefore not possible to determine individual lobe-scale flow metrics such as mean output rate and volume.

La Réunion Lava

The average wavelength for all the sampled first-generation folds across La Réunion lava flows (Table 2) was 3.8±1.8 cm. The average wavelength for all the sampled second-generation folds was 10.8±2.5 cm. The second-to-first-generation wavelength ratio for La Réunion lava was 4.6±1.2:1. Similar to the Myvatn data, it was not possible to determine meaningful volumetric measurements for the La Réunion data because of the nature of the flow field.

Discussion

Validity of the Plane Strain Assumption

In this study, we calculated apparent viscosities for six experimental lava flows using the previously described equations (Equations 2, 3a, and 4) and the GRD model (Figure 10). For each flow, apparent viscosity values calculated from Equations 2 and 4 were consistent with the GRD model (log η ~ 1-2 Pa s). Equation 3a, however, yielded extremely high apparent viscosity values for each flow (log η > 3 Pa s). Equation 3a should theoretically yield a minimum viscosity, given that it is a model used to estimate the viscosity of the flow interior, which is always lower than the crust viscosity and, therefore, the apparent viscosity of the whole flow. However, this model, based on the

original Biot (1961) model (Equation 1), assumes plane strain deformation, which does not account for significant non-coaxial strains observed on experimental lava flows. Assuming plane strain deformation in lava surface folding likely understates the total three-dimensional strain rate, and thus, overstates the apparent viscosity.

In an attempt to further understand the folding process within the context of three-dimensional strain and strain rates, we performed a video-based kinematic analysis of one experimental lava flow (Figure 11). Although this lava experiment (160331) was not included in the wavelength analysis due to poor 3D data, the vertical video data allowed for particle-tracking analysis. For this case, we thus completed a comparison of strain rate of crustal deformation in the flow-perpendicular direction to strain rates in the flow-parallel direction. In this example, flow-perpendicular strain was dominated by stretching and rotation of horizontal axis folds. The flow-perpendicular strain rate, meant only to approximate along-axis stretching of horizontal-axis folds, was 0.08 s^{-1}. For comparison, the average flow-parallel strain rate for Syracuse flows was almost two orders of magnitude lower at 0.0018 s^{-1}. This discrepancy not only illuminates the nature of non-plane strain, but also may partially explain the excessive values of apparent viscosity calculated using Equation 3a. In this equation, strain rate is inversely proportional to viscosity, thus only considering strain in two-dimensions underestimates strain rate and overestimates viscosity.

A much more rigorous analysis of non-coaxial strain rates is needed to fully quantify this effect, but these values do illustrate the nature of non-plane strain in basaltic lava crusts. In future experiments, data collection methods such as time-series

photogrammetry and thermal infrared video may help build a more quantitative assessment of the relationship between non-coaxial strain and lava rheology.

Factors affecting finite fold wavelength

Although the primary mechanism for the development of horizontal-axis folds is buckling, there are other lava flow processes that affect the geometry of these folds. Observations from experimental flows showed that topographic signals may arise on lava surfaces that mimic, or conversely, diminish the signature of both vertical- and horizontal-axis folding. One of these mechanisms, which is common to many lava flows, is inflation. Lava flow inflation occurs when a lava conduit feeds molten material into a mostly stalled flow front with a still fluid interior, resulting in uplift of the surface (Walker 1991). Inflation is common in basalt flows (e.g. Hon et al. 1994; Anderson et al. 1999; Hamilton et al. 2013), but has also been observed in more silicic flows such as the Puyehue-Cordón Caulle rhyolite flow in Chile (Farquharson et al. 2015; Magnall et al. 2017). In experimental flows, this inflation-driven surface uplift commonly occurs over a spatially variable, arcuate area with the bulk of inflation occurring near the front of the flow lobe (Figure 12). Inflation can result in stretching of the surface, unfolding folds by downslope-parallel extension. This may increase the dominant wavelengths of horizontal-axis fold trains and therefore influence rheologic interpretations. In experimental settings, this effect is easily identified and can be avoided in topographic profiling, but it may not be as noticeable in cooled natural flows. This is an example for which observations of finite strain do not accurately represent incremental strain history and can be missed in already cooled examples. At this scale, small percent changes in

wavelength may not have a large effect on rheologic interpretations, but on the scale of a more silicic flow field with meter-scale surface ridges, it could account for large changes in fold geometry. More experiments are needed to fully explain and quantify the effect of inflation on a spectral signature.

Our experimental observations also show that changes in effusion rate can affect the surface topography of a flow (Figure 13). If a folded crust is sufficiently thin, a sudden increase in lava flux can dampen fold amplitudes or even erase them completely. This appears to occur because the crust is thermally weakened and subject to gravitational collapse. If the influx is sufficient to melt the crust, all previous deformation will be erased, with no evidence preserved in the cooled flow. Observations of Syracuse lava flows showed that the latter process is common (Figure 13). Basaltic lavas, which have high strain rates relative to their cooling rates, are especially vulnerable to this mechanism, because of their limited thickening during viscoelastic deformation (Fink and Fletcher 1978; Gregg et al. 1998).

Evidence of these thermal and mechanical processes is not preserved in the final form of cooled flows; thus, they may not be accounted for in analyzing already solidified natural examples. A more informative approach to wavelength analysis would be to quantify folds in a time-series as they form. This could be performed using an array of remote-sensing techniques such as photogrammetry or laser-scanning. Studies of time-series morphology on both natural and experimental lavas have shown this technique is viable for such an investigation (e.g. Hamilton et al. 2013; Dietterich et al. 2015; Kolzenburg et al., 2018).

Multiple-generation folding

All lava flows in this study exhibit power spectra consistent with multiple-generations of horizontal-axis folding (Figure 8). This occurs when a folded crust becomes too thick to continue folding at small wavelengths (Figure 3). Because fold wavelengths are proportional to crustal thickness (Equation 1), larger wavelength folds form and are superimposed onto the previous generation of folds, which were already solidified (Gregg et al. 1998). Both analog and field experiments suggest that the ratio of subsequent wavelengths may be related to relative cooling and strain rates of the crust and thus, to lava composition and rheology (Gregg and Fink 1995; Gregg et al. 1998). Results from this study found wavelength ratios of ~5:1 for basaltic lava, in agreement with the values reported by Gregg et al. (1998) (Figure 9). Lava fold examples from La Réunion and Myvatn show this behavior. Examples from the experimental lava flows, however, display a distinctively lower wavelength ratio of ~3:1 for multiple-generation folding. Because all the lava flows studied exhibited limited crystallinity and vesicularity, two major controls on rheology, compositional differences likely account for the wavelength ratio disparity between natural and experimental lava.

Our experimental lavas fall within the compositional range of basaltic andesite (~54% SiO_2) whereas Iceland and La Réunion lavas are basalts (~50% SiO_2) (Table 1). A wavelength ratio of 3:1 corresponds to previously reported ratios between basalt (~5:1) and andesite (~2:1) (Gregg et al. 1998) (Figure 9). Gregg et al. (1998) hypothesized that silicic lavas were distinct from basalts in terms of wavelength ratios but did not suggest a spectrum of ratios between the compositions. The intermediate composition of basaltic andesite presented in this study bridges the gap between silicic

and basaltic lavas reported in Gregg et al. (1998). Furthermore, the wavelength ratios plotted against SiO_2 content are suggestive of a power-law relationship (Figure 9). SiO_2 content is only a very rough approximation of total rheology, but the correlation is notable.

The correlation between wavelength ratios and lava types is also supported by the GRD viscosity model results for natural and experimental lavas (Figure 10b). Myvatn and La Réunion lavas have very similar temperature-viscosity curves, due to their similar compositions, and both display wavelength ratios of ~5:1. The Syracuse alkali lava flow (Syracuse 1) exhibits slightly higher viscosity than the basalts and also a slightly lower wavelength ratio of ~4:1. Model results for all other Syracuse lavas show an intermediate viscosity curve between the basalts (Myvatn, La Réunion) and andesite, consistent with a smaller wavelength ratio of ~3:1. Extrapolating even further, the viscosities of dacite and rhyolite are the highest based on GRD model results and are thus consistent with low (< 2:1) wavelength ratio results from previous studies (Gregg et al. 1998; Lescinsky et al. 2007; Pyle and Elliott 2006).

Although wavelength ratio uncertainty is high for lavas reported thus far, further refinement and more data may lead to a predictive model wherein lava flow compositions could be approximated based on the geometry of their folded surfaces. A model such as this would be of considerable value in the fields of planetary and marine geology, where imagery is common but sampling and chemical analyses are limited or not available. Another advantage of the wavelength ratio model is that it does not rely on the typical physical parameters such as thickness, density, mean output rate, or velocity, which can be difficult or impossible to measure in ancient or distant flows. As

shown in this and other studies, determining wavelength ratios requires only topographic data, which can be produced using photogrammetry, laser and radar scanning, or total station surveys (Favalli et al. 2018; Gregg et al. 1998; Lescinsky et al. 2007; Pyle and Elliott 2006).

Other rheologic controls of lava, such as crystallinity, vesicularity, and underlying topography, must all be considered in any interpretation of lava in the lab or in the field. In future experiments, it may be informative to test the influence of these variables individually on the incremental and finite fold geometry of a flow surface. Since wavelength ratios are not an exact a proxy for composition, but for relative strain and cooling rates, these factors must be quantified in any attempt at a fully informative analytical model. This could be achieved in future experiments by utilizing thermal camera and thermocouple data, which have been proven as successful techniques in the field and in the lab (e.g. Harris et al., 2005; Harris et al., 2007; Lev et al., 2012).

Conclusions

High-resolution digital topography allows for the quantification of fine-scale features of lava flow crusts. Fourier analysis identifies distinct wavelength patterns for horizontal-axis fold trains on natural and experimental lava flows. Spectral results exhibit patterns consistent with multiple-generation horizontal-axis folding along flow surfaces. Second-to-first generation fold wavelength ratios of ~5:1 for basalt and ~3:1 for basaltic andesite are in agreement with previous studies of natural flows.

Video analysis of experimental lava flows reveals previously undescribed aspects of fold evolution and strain history of the crust. Vertical-axis folding, resulting from

viscosity and velocity gradients normal to the flow direction, deform earlier horizontal-axis folds, violating the assumption of plane strain used in some rheological models.

Other processes such as flow inflation and thermal relaxation of the crust are also likely to modify fold geometry and thus, the spectral signal of topography. Observations of experimental lava flows, from which incremental strain history can be evaluated, reveal complexities that are generally not accounted for in studies of finite strain from the profiles of folded surfaces of cooled flows.

The complexities identified in this study caution us in our interpretation of the strain history of lava flows for which active flow has not been directly observed in the field. However, the fold analysis methodology presented in this study confirms that, despite these complications, a correlation exists between fold wavelength ratios and lava composition and rheology, regardless of complex strain history.

Tables

Table 1. Normalized major element compositions in wt.% for lavas analyzed in this study.

Sample	SiO_2	Al_2O_3	FeO	MgO	CaO	Na_2O	K_2O	TiO_2	MnO	P_2O_5	Total	Citation
Syracuse	54.13	15.78	9.48	6.36	8.37	2.80	0.86	1.89	0.19	0.15	100.00	This study
Syracuse Alkali	53.19	15.38	8.70	6.19	8.09	4.64	1.68	1.83	0.17	0.13	100.00	This study
Myvatn	50.28	13.15	15.00	5.64	10.49	2.48	0.34	2.13	0.25	0.24	100.00	Grönvold, 1984
La Réunion	49.20	13.96	11.31	8.04	11.11	2.63	0.66	2.59	0.17	0.32	100.00	Vlastélic et al., 2007

Table 2. Wavelength analysis results for the 16 lava flows analyzed in this study.

Flow	λ_1 (cm)	2σ	λ_2 (cm)	2σ	Ratio	2σ	DEM horizontal resolution (mm)	DEM vertical accuracy (mm)	Strain	RMS amplitude (cm)	Composition
Syracuse 1	0.8	0.3	3.1	0.1	4.2	1.0	0.2	0.1	-0.35	0.19	Syracuse Alkali
Syracuse 2	1.2	0.1	2.8	0.3	2.4	0.4	0.4	0.3	-0.22	0.20	Syracuse
Syracuse 3	1.3	0.1	4.7	0.4	3.5	0.3	0.1	0.1	-0.28	0.34	Syracuse
Syracuse 4	1.4	0.1	4.4	0.2	3.2	0.3	0.3	0.3	-0.26	0.39	Syracuse
Syracuse 5	0.8	0.1	2.4	0.1	2.8	0.2	0.3	0.1	-0.17	0.14	Syracuse
Syracuse 6	1.3	0.1	3.4	0.5	2.6	0.6	0.3	0.1	-0.31	0.19	Syracuse
Syracuse 7	1.3	0.0	4.8	0.8	3.5	0.6	0.2	0.1	-0.17	0.23	Syracuse
Syracuse 8	1.1	0.0	3.5	0.3	3.1	0.2	0.2	0.2	-0.35	0.41	Syracuse
Myvatn 1	2.1	0.3	12.8	0.8	6.3	0.7	0.4	0.0	-0.22	0.95	Myvatn
Myvatn 2	2.1	0.2	9.4	0.9	4.6	1.0	0.4	0.1	-0.14	0.37	Myvatn
Myvatn 3	1.8	0.2	8.0	0.7	4.6	0.8	0.4	0.1	-0.13	0.27	Myvatn
Myvatn 4	2.2	0.4	12.2	0.0	5.7	1.2	0.3	0.1	-0.18	0.46	Myvatn
Myvatn 5	1.7	0.1	7.0	0.6	4.1	0.4	0.4	0.1	-0.20	0.33	Myvatn
La Réunion 1	2.8	0.8	12.3	1.1	4.6	1.4	0.3	0.1	-0.26	0.52	La Réunion
La Réunion 2	1.9	0.1	9.9	1.5	5.2	0.8	0.5	0.3	-0.20	0.54	La Réunion
La Réunion 3	2.9	0.9	11.3	0.9	4.0	1.7	0.5	0.1	-0.19	0.73	La Réunion

Table 3. Physical parameters and apparent viscosities calculated for Syracuse lava flows using DTMs and video analysis.

Flow	Slope angle (°)	+/-	Max T (°C)	+/-	Mean thickness (cm)	+/-	Max velocity (cm/s)	+/-	Area (m^2)	+/-
Syracuse 1	10	0.5	1394	28	2.7	0.1	9	1	1.6	0.1
Syracuse 2	5	0.5	-	-	1.6	0.1	-	-	0.9	0.1
Syracuse 3	12	0.5	1312	26	2.6	0.1	3	1	0.5	0.1
Syracuse 4	12	0.5	1291	26	3.0	0.1	5	1	1.3	0.1
Syracuse 5	6	0.5	1344	27	2.2	0.1	6	1	0.7	0.1
Syracuse 6	7	0.5	1324	26	3.1	0.1	6	1	1.0	0.1
Syracuse 7	3	0.5	1332	27	5.2	0.1	7	1	1.2	0.1
Syracuse 8	3	0.5	-	-	3.7	0.1	-	-	1.2	0.1
x̄	-	0.5	1333	27	3.0	0.1	6	1	1.0	0.1
1σ	-	0.0	35	1	1.1	0.0	2	0	0	0

Flow	Volume (cm^3)	+/-	Flux (cm^3/s)	+/-	Log η_1 (Pa s)	+/-	Log η_2 (Pa s)	+/-	Log η_3 (Pa s)	+/-	Log η_4 (Pa s)	+/-
Syracuse 1	4.3E+04	120	260	10	0.8	0.7	3.0	1.4	0.9	0.3	1.2	0.1
Syracuse 2	1.3E+04	230	-		-	-	-	-	-	-	-	-
Syracuse 3	1.2E+04	25	110	10	1.2	0.7	3.0	1.4	1.5	0.4	1.7	0.1
Syracuse 4	3.9E+04	410	280	10	1.1	0.6	2.6	1.6	1.4	0.3	1.8	0.1
Syracuse 5	1.4E+04	40	120	10	0.5	0.9	3.7	0.9	0.6	0.4	1.5	0.1
Syracuse 6	3.0E+04	90	150	10	1.2	0.6	3.9	0.7	1.1	0.3	1.6	0.1
Syracuse 7	6.4E+04	100	160	10	1.8	0.3	3.9	1.0	1.1	0.2	1.6	0.1
Syracuse 8	4.5E+04	270	-	-	-	-	-	-	-	-	-	-
x̄	3.3E+04	160	180	10	1.1	0.6	3.4	1.2	1.1	0.3	1.6	0.1
1σ	1.9E+04	130	70	0	0.4	0.2	0.6	0.3	0.3	0.1	0.2	0.0

Figures

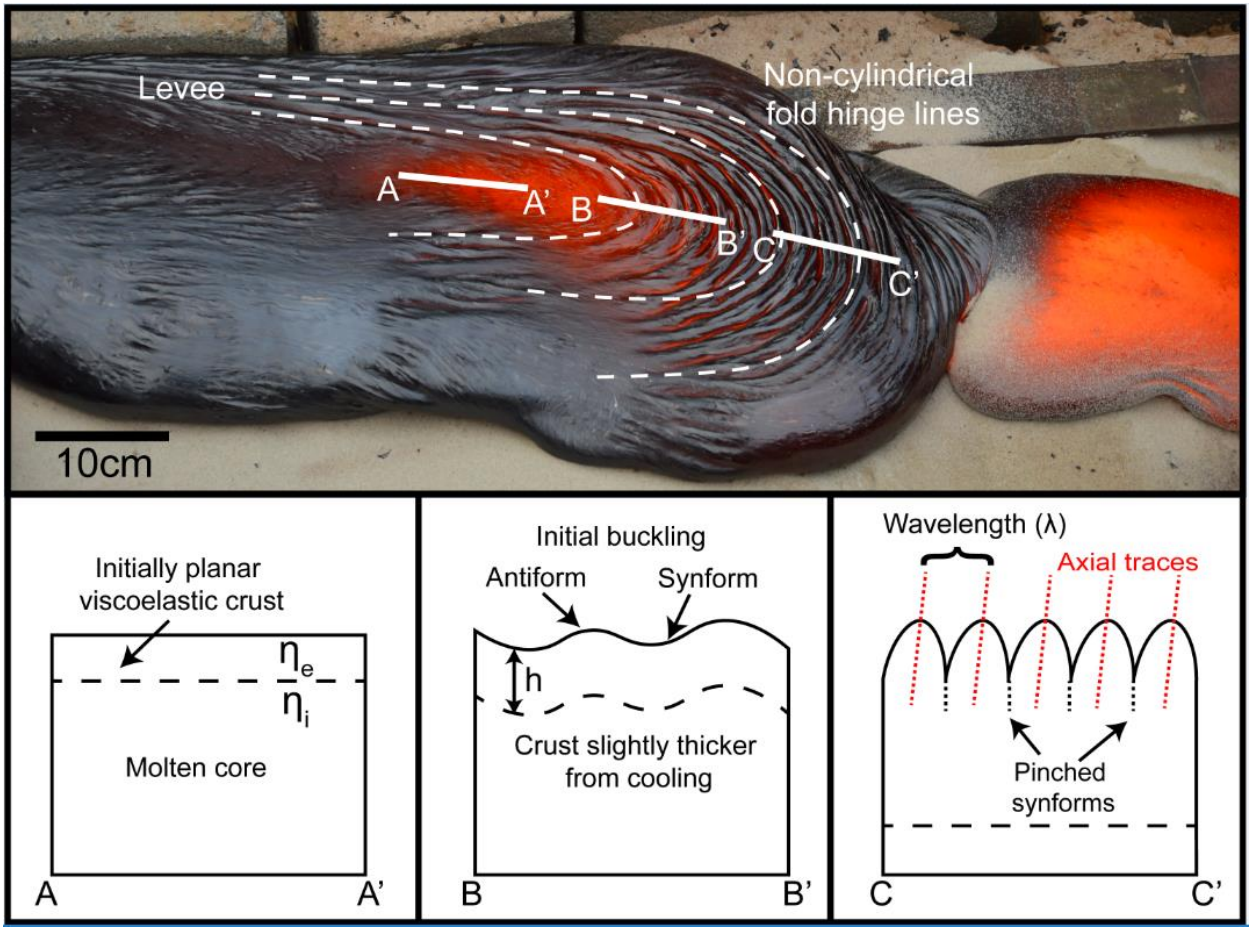

Figure 1. Oblique view of experimental lava lobe with a single generation of horizontal-axis folds and schematic cross sections. A-A' – initial conditions, showing a planar viscoelastic crust with thickness h coupled to a molten core where ηe is crust viscosity and ηi is core viscosity. B-B'– onset of crustal buckling, crustal thickness changes due only to cooling. C-C'¬– finite, two-dimensional strain showing a fold train of antiforms and pinched synforms preserving a dominant, single-generation wavelength (λ) pattern. Crustal thicknesses are greatly exaggerated.

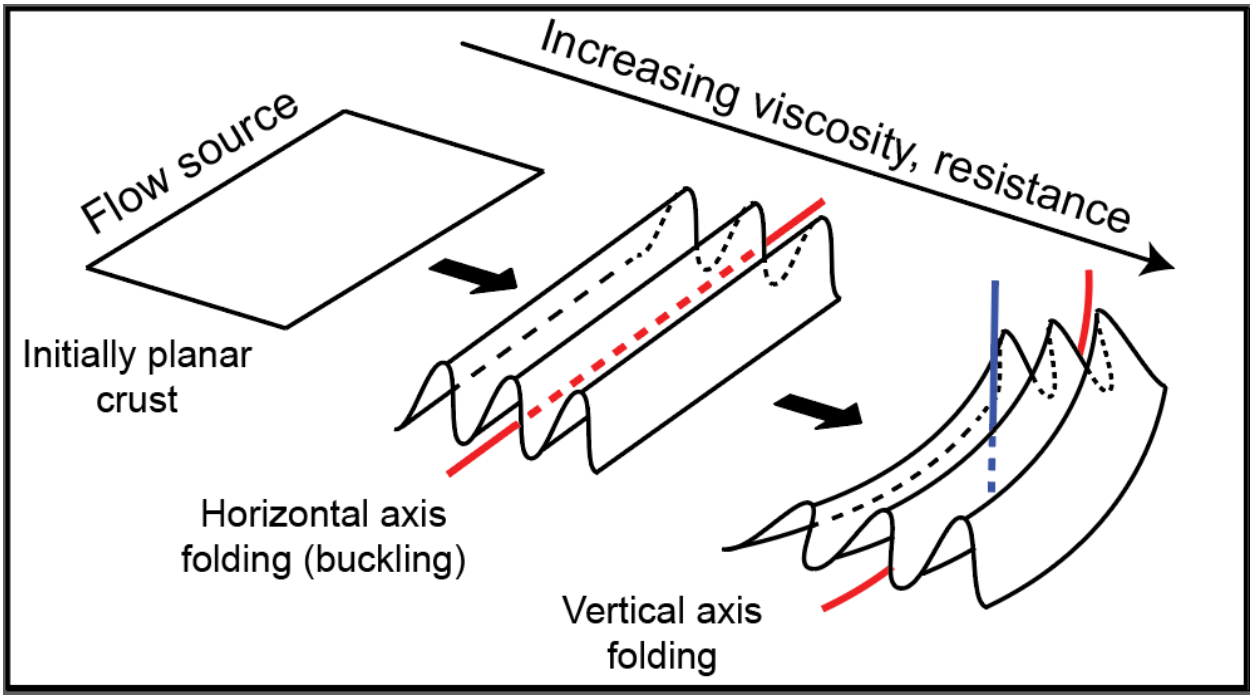

Figure 2. Simplified diagram representing two different fold geometries observed in lava flows: horizontal- and vertical-axis folds. Thick arrows give flow direction and downslope-directed stress. Red and blue lines mark hinge lines for horizontal- and vertical-axis folds, respectively.

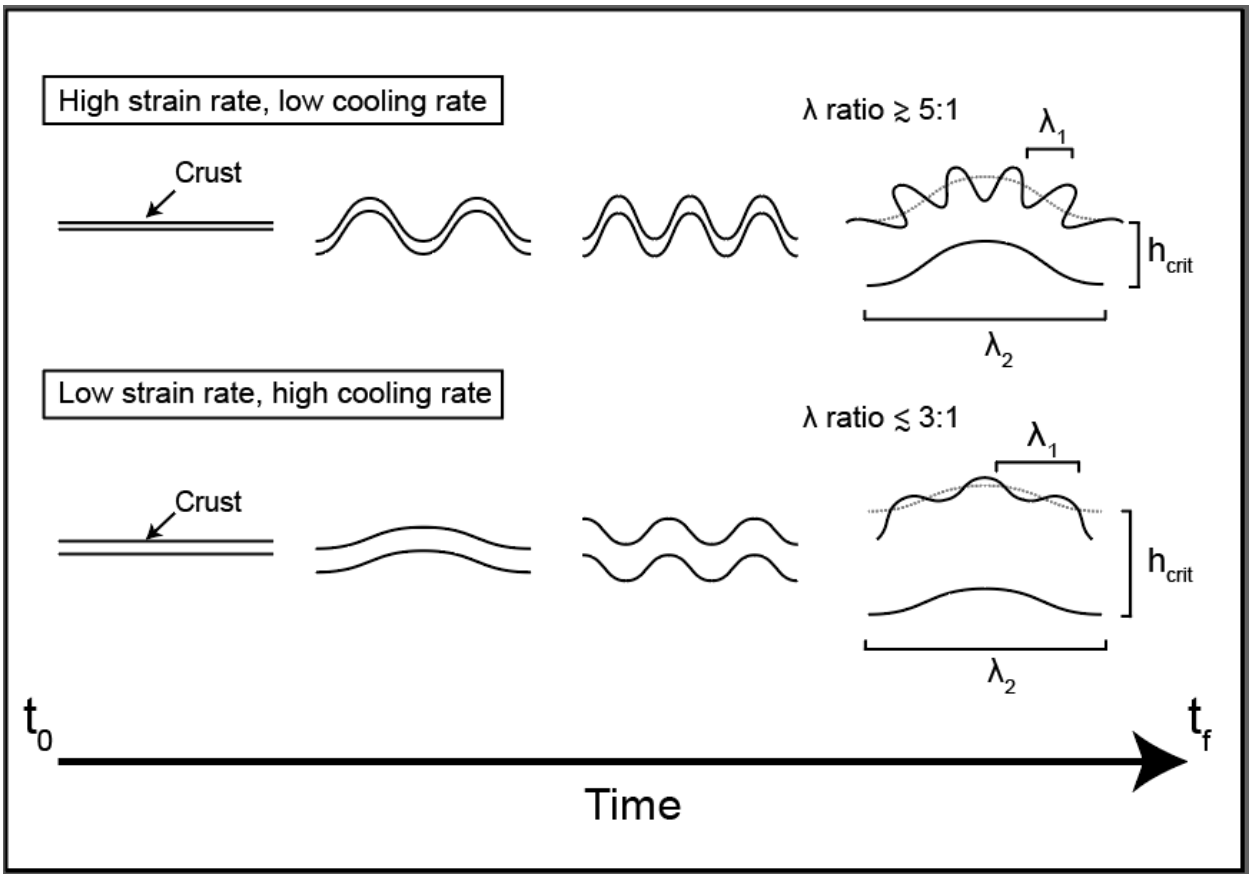

Figure 3. Simplified sketch of multiple-generation horizontal-axis folding. λ_1 – first-generation fold wavelength; λ_2 – second-generation fold wavelength; h_{crit} – critical crustal thickness at which second-generation folds appear; t_0 – time of crust formation; t_f – time of solidification. Top time-series - folding for a lava with high strain rate, relative to cooling rate (typical of basalt flows); this typically results in a high wavelength ratio. Bottom time-series - folding for a low strain rate lava (typical of more silicic flows); this typically results in a low wavelength ratio.

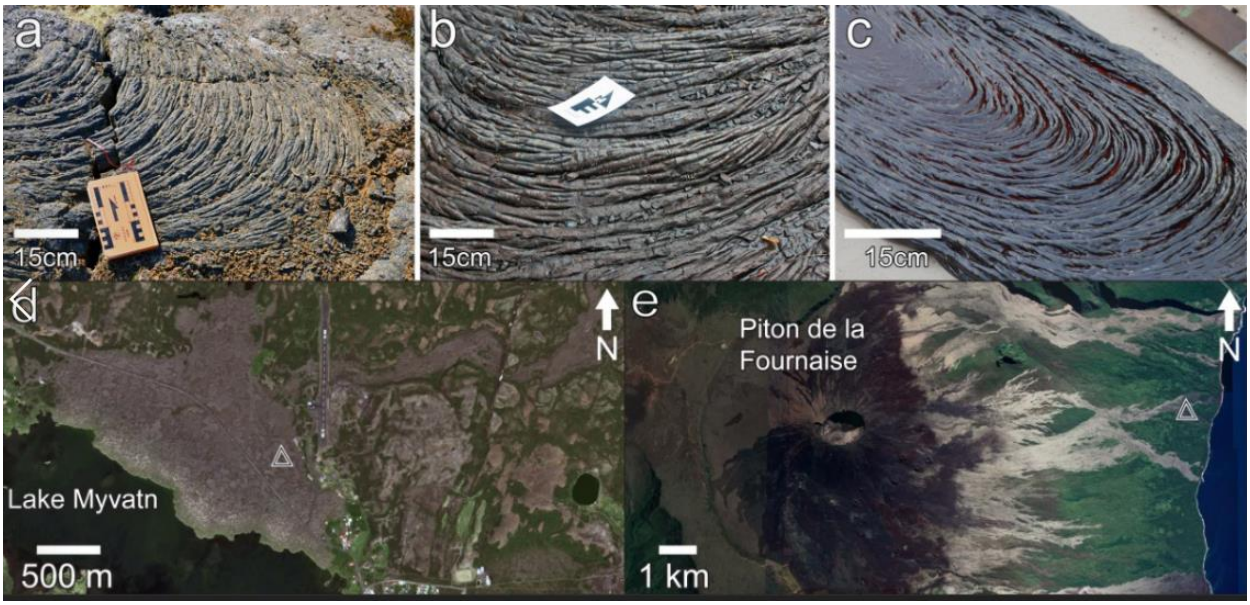

Figure 4. Examples of lava flows from **a** Myvatn, Iceland (basalt), **b** La Réunion Island (basalt), and **c** Syracuse University Lava Project (basaltic andesite). Location maps for **d** the Myvatn and **e** Piton de la Fournaise lava fields. Triangles – location of field sites. Map data: Google, DigitalGlobe.

Figure 5. High-volume, gas-fired tilt furnace used for melting batches of basaltic- to basaltic-andesite lava at the Syracuse University Lava Project.

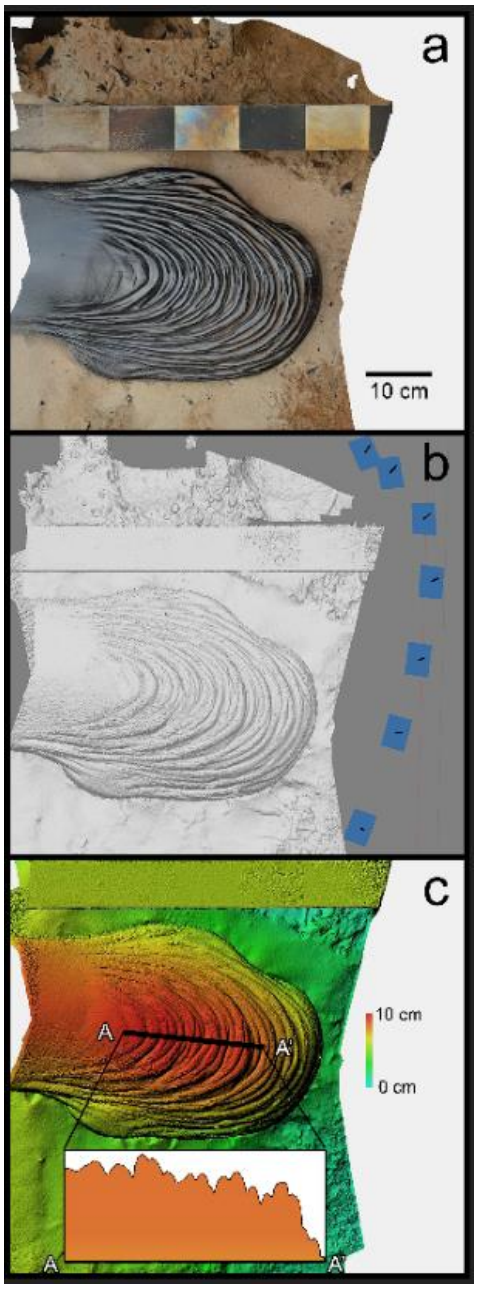

Figure 6. Workflow methodology for extracting topographic profiles across lava flows. **a** Orthophotograph of lava lobe from the Syracuse University Lava Project; scale bar divisions are 10 cm. **b** Structure-from-Motion 3D point cloud with camera locations (blue boxes), processed in Agisoft Photoscan®. **c** Digital terrain model of lava lobe, built from 3D point cloud in Agisoft Photoscan® with topographic profile (A-A').

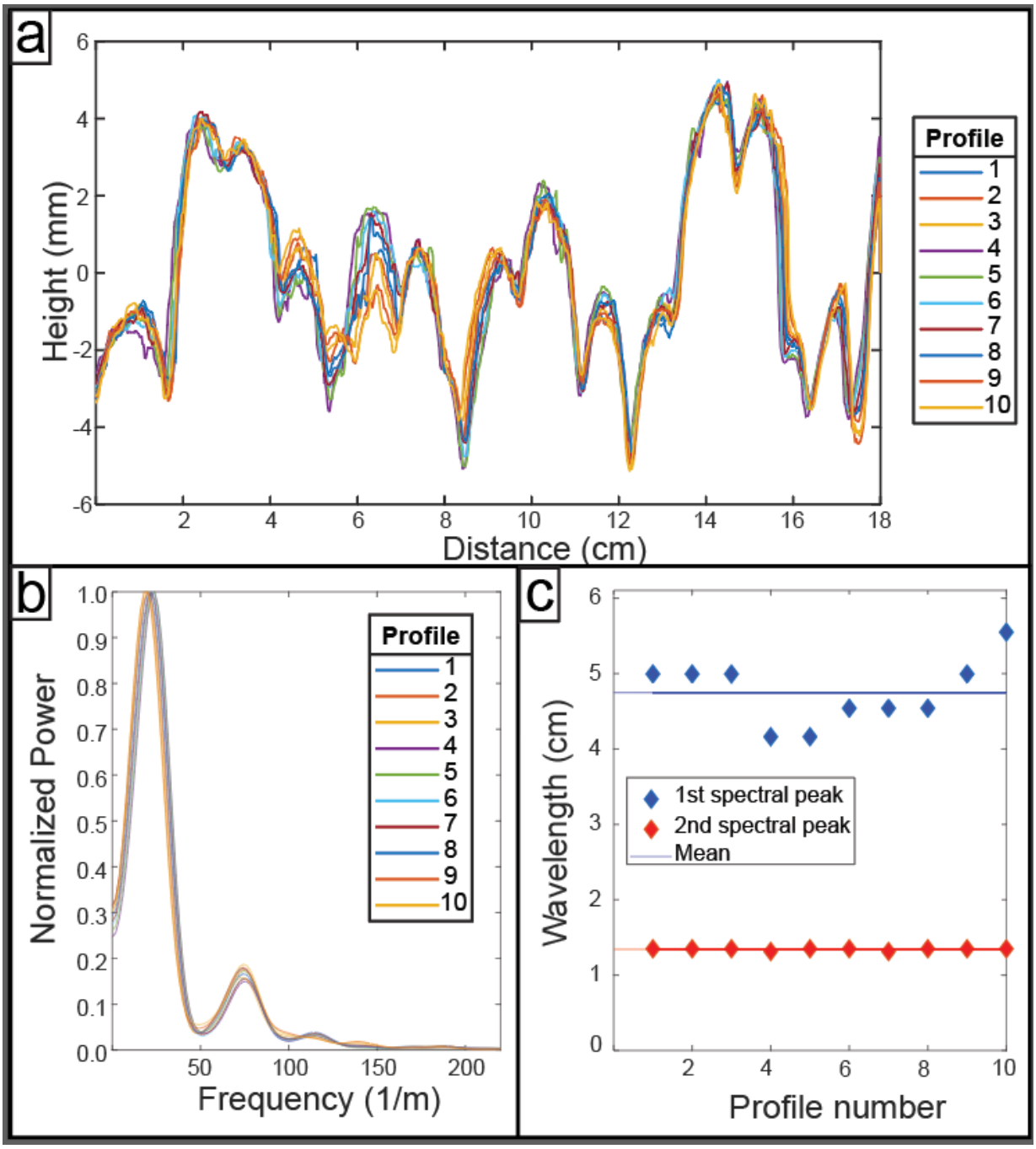

Figure 7. Workflow for extracting dominant wavelength patterns along a folded lava surface. **a** Ten topographic profiles along flow Syracuse 7. **b** Power spectrum of each topographic profile. **c** Spectral peaks from power spectra, converted to wavelength. The first spectral peak corresponds to second-generation (large wavelength) folds and the second spectral peak corresponds to first-generation (small wavelength) folds.

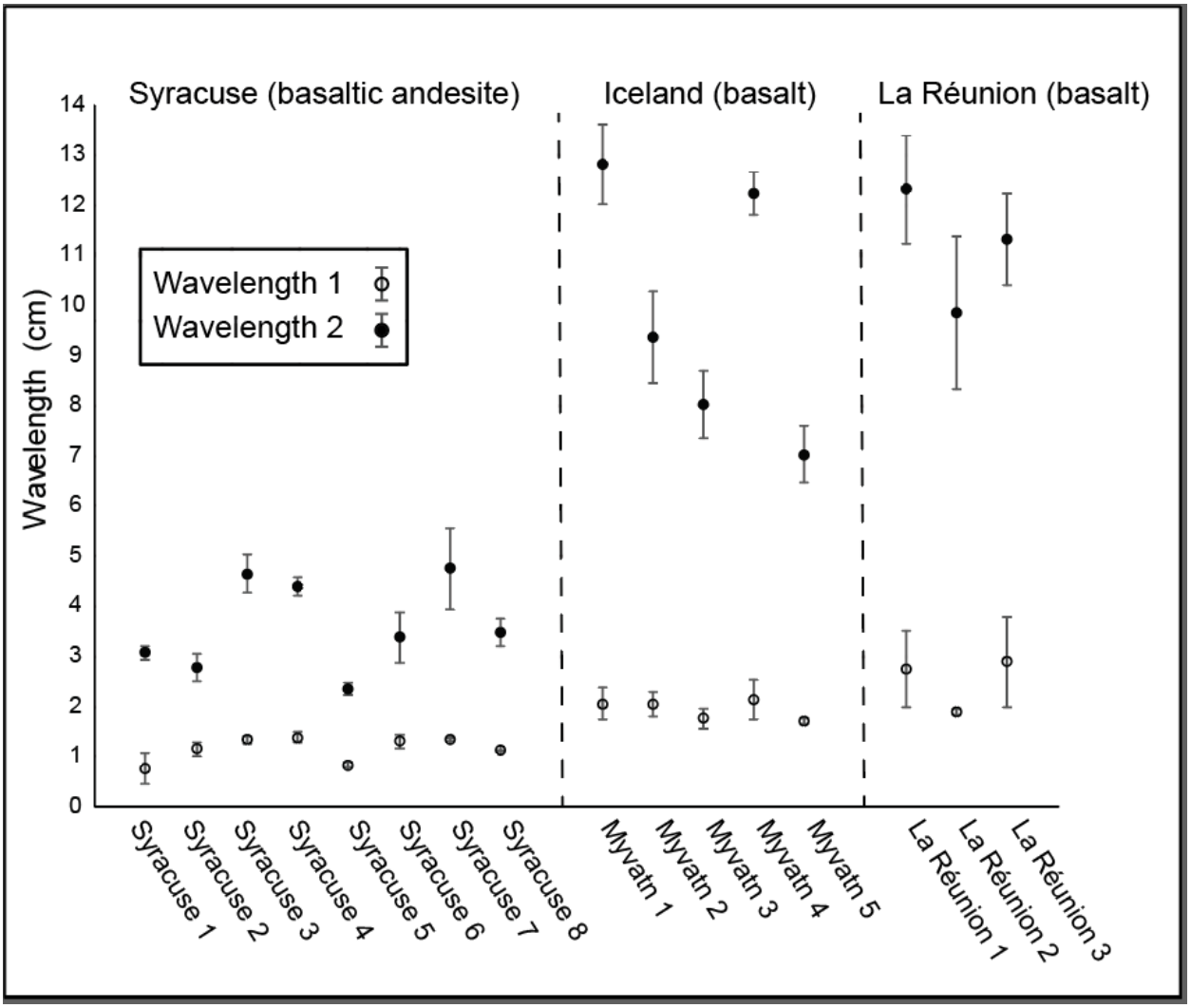

Figure 8. Average wavelength picks for experimental and natural lava flows. Error bars are 2σ uncertainty.

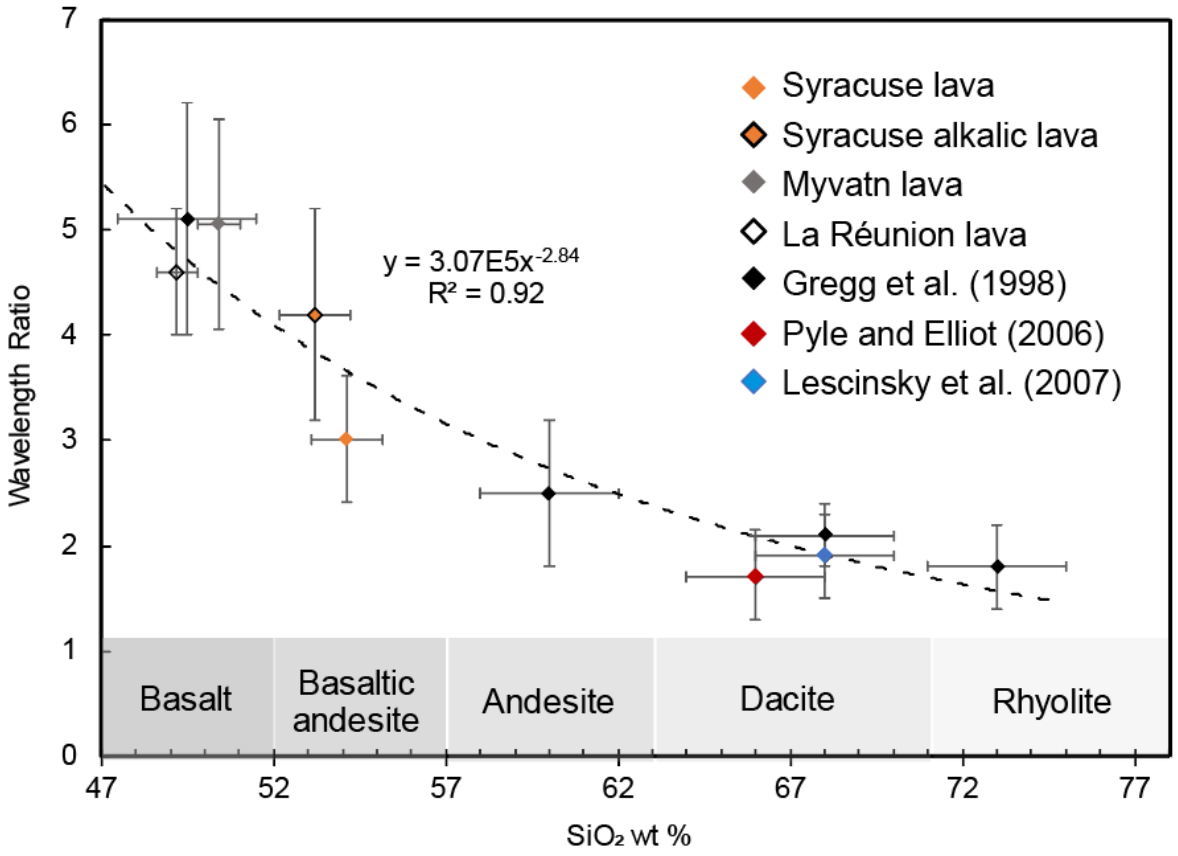

Figure 9. Wavelength ratios for multiple-generation horizontal-axis folds among different types of lavas plotted against SiO_2 content. Error bars are the total range of measured values.

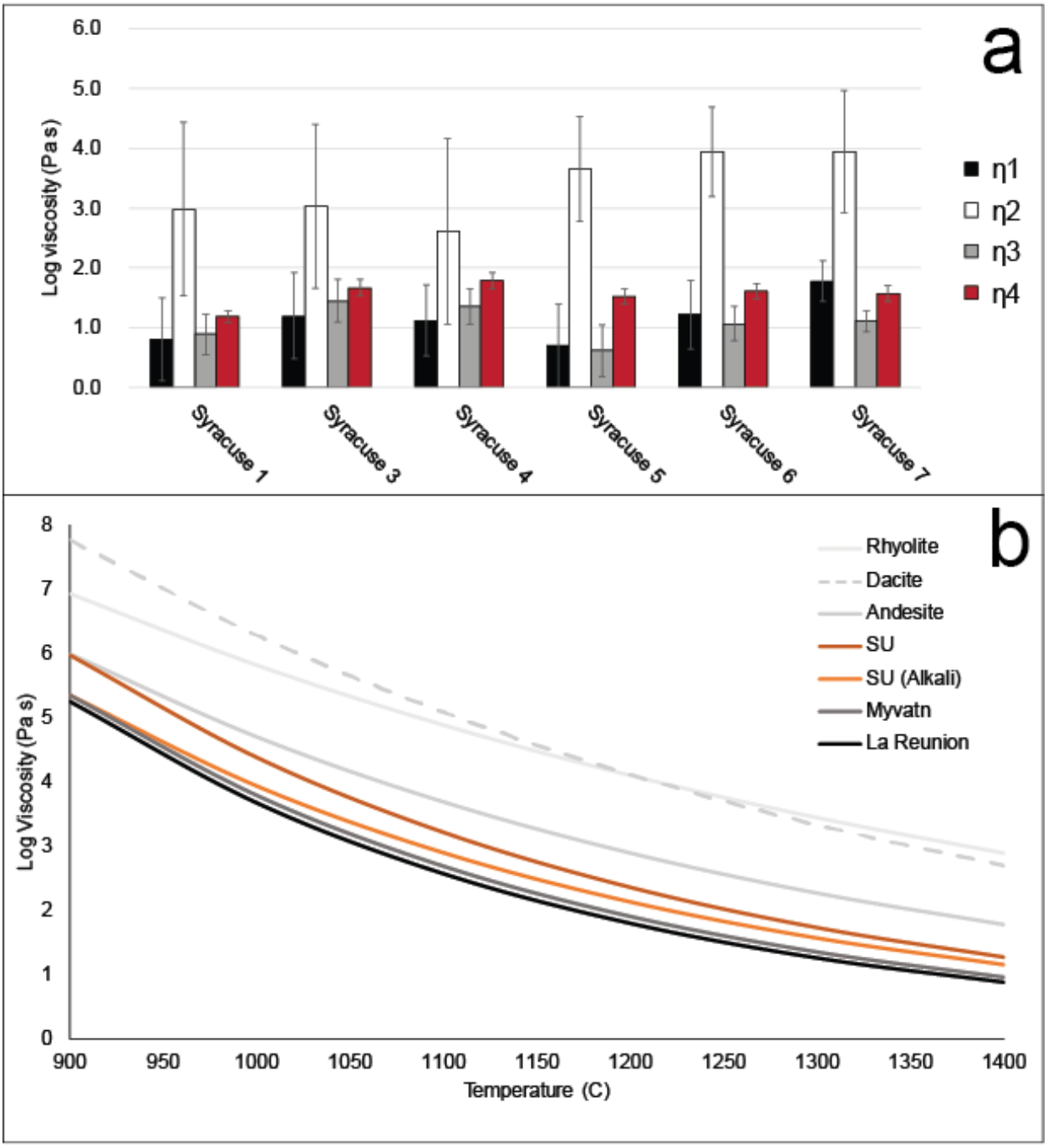

Figure 10. Apparent viscosity model results of lava flows. Error bars are the total range of calculated values. **a** Apparent viscosities based on equations 2 (η1), 3a (η2), 4 (η3), and the GRD model (η4). **b** Temperature-viscosity curves for selected lavas, calculated using the GRD model as a means for comparing lava types.

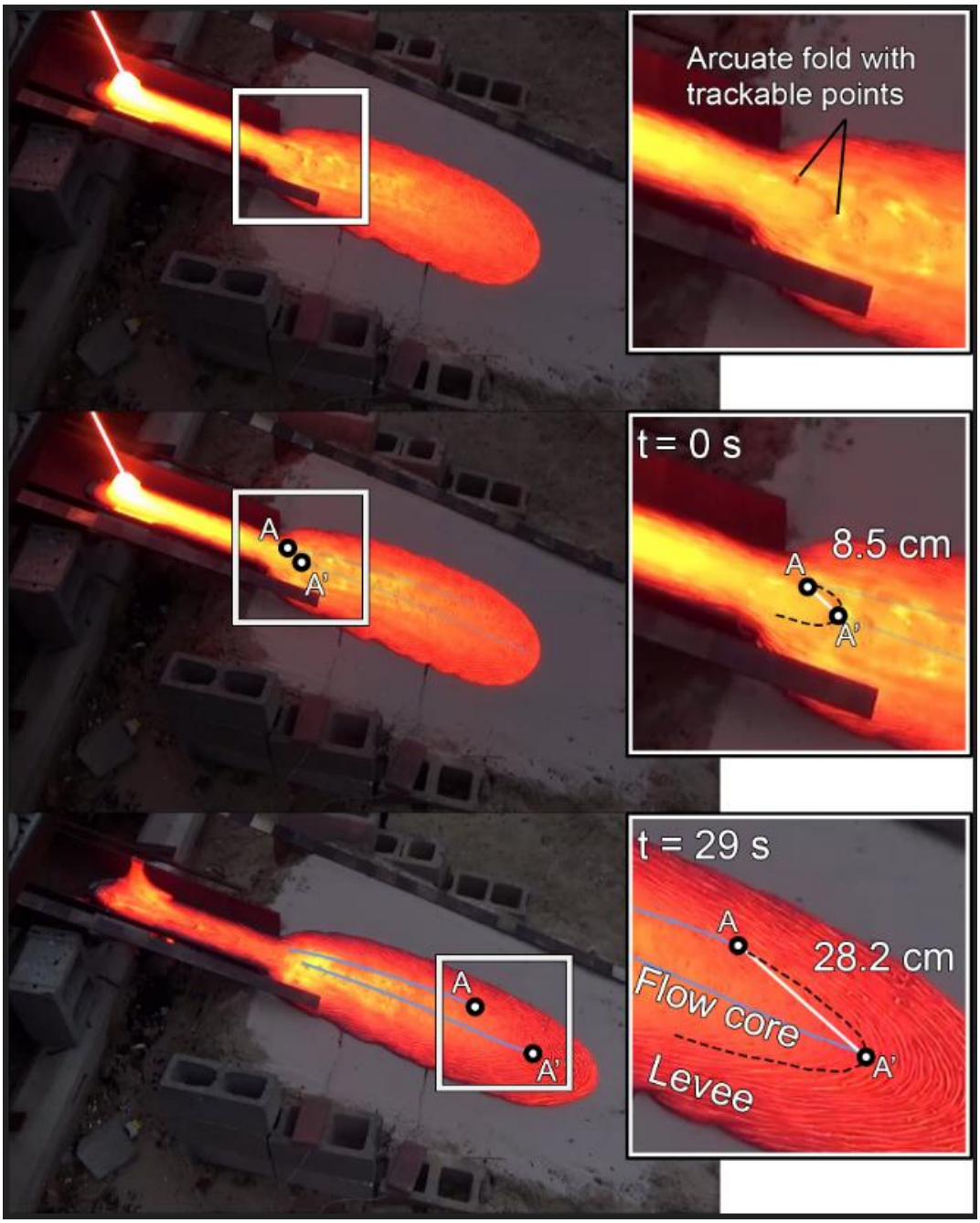

Figure 11. Kinematic video analysis of a Syracuse lava flow with areas indicated by the white boxes enlarged on the right. Points A and A' are trackable points along horizontal-axis fold. Initial point separation is 8.5 cm; point separation at t= 29 s is 28.2 cm. Separation of A-A' is proportional to the magnitude of along-axis stretching of the horizontal-axis fold, a process that creates vertical-axis folds and levees.

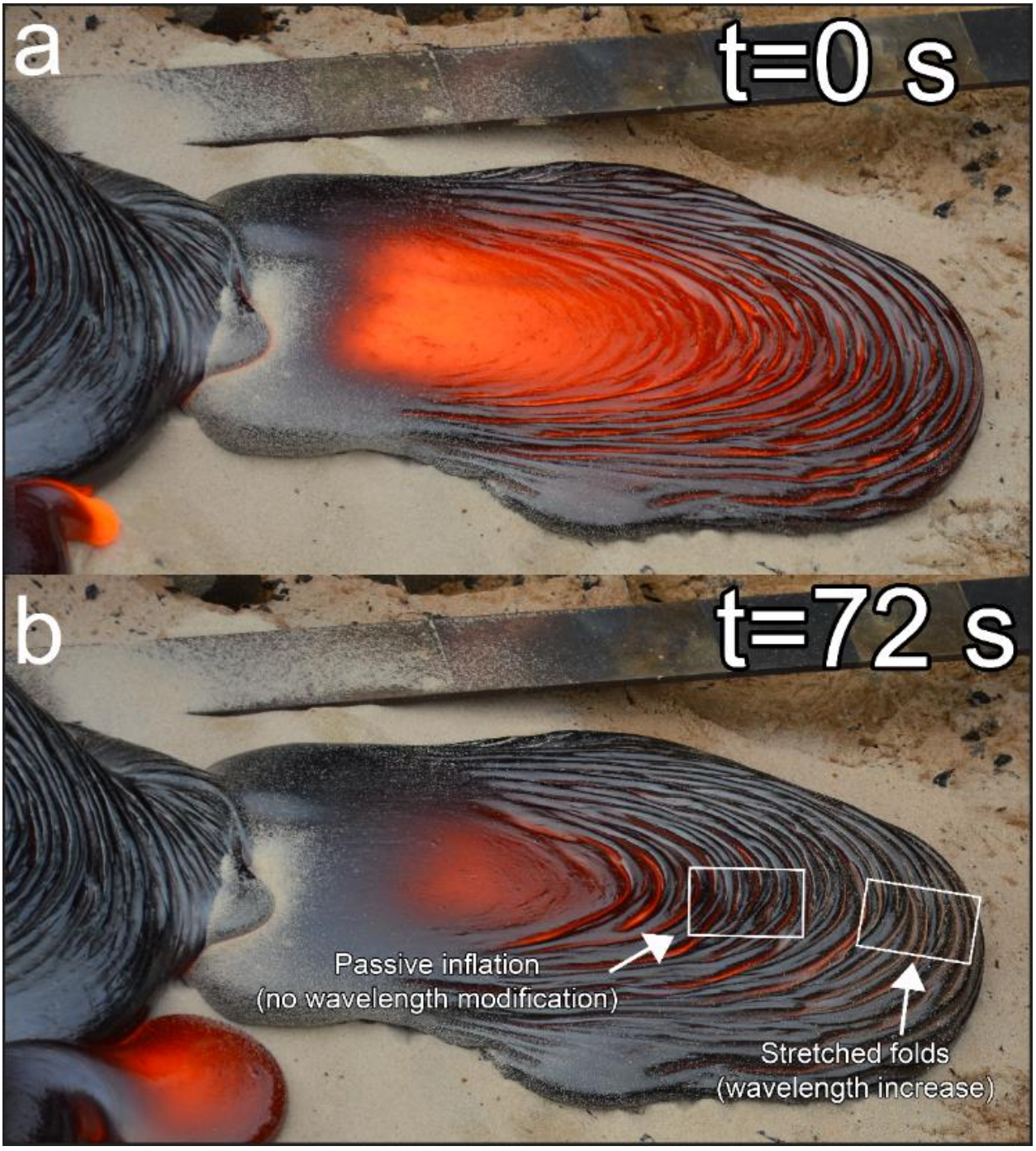

Figure 12. Flow Syracuse 7, frontal toe used for wavelength analysis. Scale bar divisions are 10 cm. **a** Toe during initial organization of dominant fold trains. **b** Toe after inflation, showing modification of surface topography.

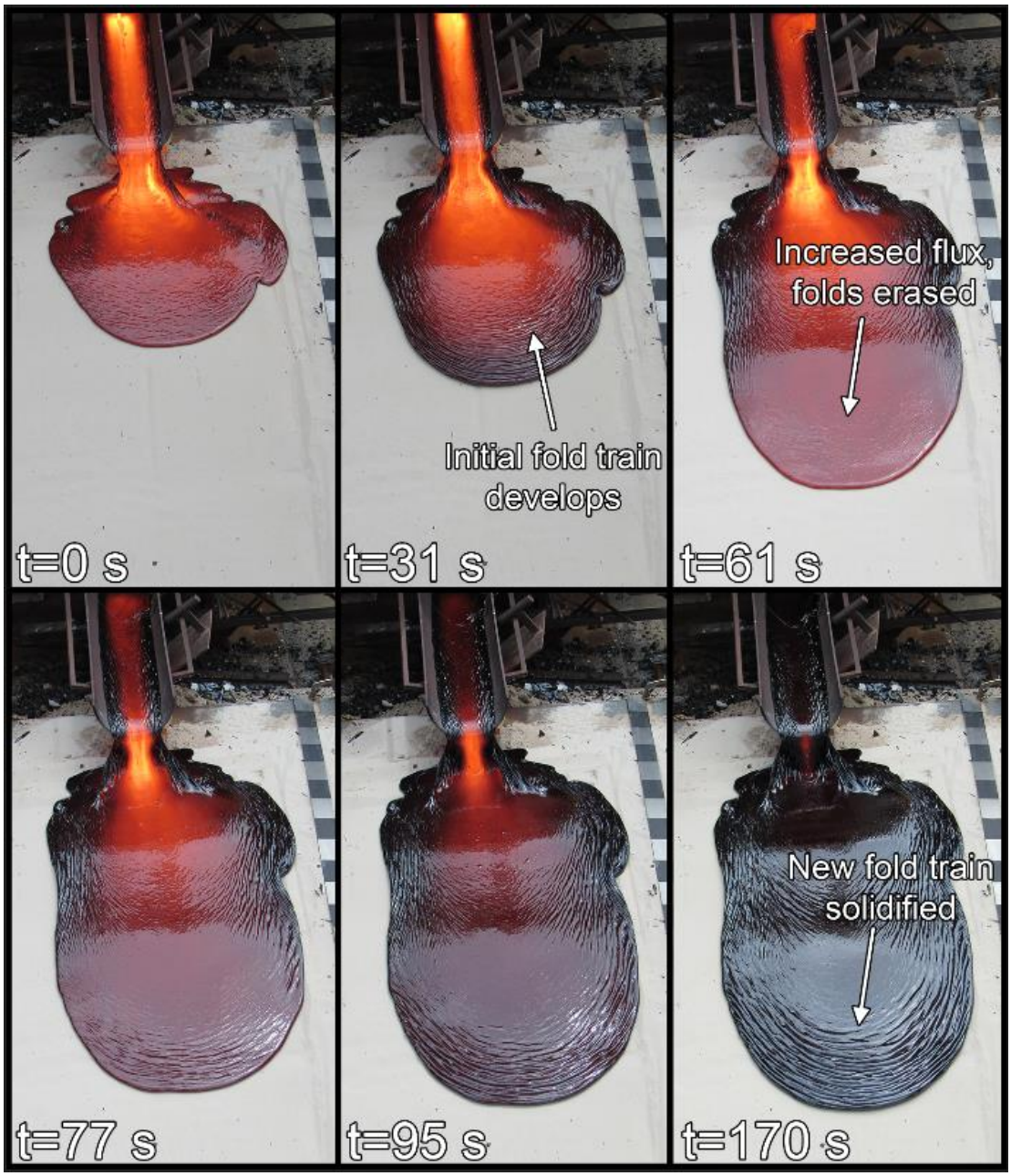

Figure 13. Example of crustal folding and subsequent erasure of folds. Scale bar divisions are 10 cm. Fold trains initially organize into dominant wavelengths as crust cools. At t=61 s, increased effusion rate causes thermal weakening, or possibly melting, of folded crust, erasing evidence of mid-flow crustal strain. By t=95 s, new fold trains organize, and a new dominant wavelength prevails, with no preservation of previously erased folds.

Chapter 2: Mapping the 4-dimensional viscosity field of an experimental lava flow

In preparation for submission to:

Journal of Geophysical Research: Solid Earth

Abstract

Viscosity is a critical rheologic parameter that determines the behavior, evolution, and final morphology of active lava flows. Measuring the viscosity of a lava flow, however, is non-trivial. The rheologic structure of lava is complex, and during active flow conditions, viscosity can change by orders of magnitude through space and time. This makes viscosity one of the most elusive properties of flowing lava. Nevertheless, after almost a century of lava viscometry, it is still common practice to reduce a flow viscosity to a single value, generalizing an immense field of deviations and complexities. Considering lava viscosity as a 1-dimensional variable may be sufficient for characterizing some aspects of flows but it does not allow for solving higher-order rheological problems, such as depth structure, spatial variability, or rates of change. This study goes beyond traditional viscometry by solving for the 4-dimensional viscosity field of an actively flowing experimental lava. Results from this experiment include time-series viscosity maps of the lava flow with a spatial resolution of 1 cm^2. Additionally, the viscometry approach used in this study allows for an analysis of vertical rheologic structure, specifically, crust and core viscosity layers. Although this study was performed in an experimental setting, the basic data collection techniques applied are common in field volcanology and thus could be applicable in certain natural settings.

Introduction

Effusive volcanism represents one of the primary resurfacing mechanisms for terrestrial planets and moons in the solar system. The products of this mechanism are lava flows, thus, understanding the dynamics of flowing lava has implications for interpreting the evolution of volcanically active planets and planetary bodies. Additionally, on Earth, lava flows can represent a significant natural hazard to populations living within volcanically active regions. Resolving the dynamics of lava flow behavior can help inform crisis management techniques such as monitoring and hazard mapping.

Lava flows advance and evolve as a function of rheology and the surrounding environment (e.g., topography). One of the primary rheologic factors determining the advance rate of a lava flow is the lava viscosity. Low-viscosity lavas can flow rapidly, even on relatively shallow slopes of 5° or less. Eruptions at Goma in 2002 and Kilauea in 2018 produced basaltic lava flows that traveled up to and exceeding ten meters per second (Giordano et al. 2007; Tedesco et al. 2007). High-viscosity lavas advance much more slowly but can also pose significant hazards. High-viscosity lava domes, for example, grow at very slow rates, but can collapse dramatically and trigger pyroclastic density currents (Newhall and Melson 1983; Sparks 1997). Thus, understanding the temporal- and spatial-dependent rheology of all lava systems is of critical importance for hazard management.

Many studies have advanced the field of active lava flow viscometry through observations of natural, experimental, and analog flows. It has become common practice, however, to reduce lava viscosity to a single value, even though it is known

that lava viscosity spans orders of magnitude across and over the duration of a single flow. A 1-dimensional value for viscosity can be useful for comparative volcanology but is not representative of the complex dynamic rheology of an evolving active lava flow. The goal of this study is to determine, for the first time, the temporal and spatial viscosity field of an experimental basaltic lava flow and discuss how these results may be relevant for natural lava flows.

History of Viscometry

Lava flow viscometry has foundations in Nichols (1939), who first attempted to constrain the viscosity of lava using the Jeffreys (1925) equation (described in detail below) for viscous laminar flow down a slope. Using this model, which assumes Newtonian flow, Nichols (1939) estimated the viscosity of a Hawaiian lava flow to be about 4.3 to 4.8 x 10^3 Pa s. Morphometric approaches, such as the Jeffreys equation, yield a value termed *apparent viscosity*, which incorporates the depth-averaged rheology of the heterogenous lava flow (Griffiths 2000). Although lava flows exhibit complex rheological layering, including rapidly evolving viscoelastic and brittle crust layers, apparent viscosity is a useful value for comparative purposes (Hon et al. 1994). Since the study by Nichols (1939), the Jeffreys equation (and its derivatives) has become a standard for estimating the apparent viscosity of active lava flows in the field and in the lab (e.g. Farquharson et al. 2015, Lev et al. 2012; Gregg and Fink 2000).

In parallel to the development of morphometric approaches for apparent lava viscosity, many studies have focused efforts on laboratory and numerical solutions for

the *melt viscosity* of lava. Melt viscosity, in contrast to apparent viscosity, considers only the dynamics of the homogenous fluid in a lava, which exhibits a strong control on the total rheology (Griffiths 2000). In natural lava flows, melt viscosity primarily influences the motion and behavior of the viscous core, but can also be used to describe the dynamics of the viscoelastic crust (e.g.,Giordano et al. 2008). Early work by Bottinga and Weill (1972) and Shaw (1972) showed that melt viscosity is dependent on both temperature and major element composition. This empirical study led to a procedure for calculating the temperature-viscosity relationship for a silicate melts given the major element composition (Shaw 1972). The Shaw (1972) model is still used in modern studies and shows good agreement with physical measurements under a specific range of conditions (Fink and Zimbelman 1986; Lev et al. 2012; Marsh 1981). Although it remains a powerful tool for melt viscosity modeling, Giordano and Dingwell (2003) described the limitations of the Shaw (1972) model and showed the it breaks down for melts of high volatile content (> 2%) and outside the range of temperatures between 1050° – 1150° C. Building upon this work, Giordano et al. (2008) developed a new melt viscosity model that incorporates volatile content, as well as temperature and composition, to predict the melt viscosity of lavas. This model is based on over 1700 laboratory viscometry measurements of silicate melts and can accurately predict melt viscosity across 15 orders of magnitude (10^{-1} - 10^{14} Pa s) (Giordano et al. 2008). The model, referred to herein as GRD, is widely used in volcanology and is a standard for calculating melt viscosity (Giordano et al. 2008).

Calculating the viscosity of lava using any approach requires accurate measurements of morphologic, kinematic, and thermal variables. Measuring these

parameters is far from trivial, given the inherent dangers associated with field work in volcanic environments. In a few instances, researchers have been able to measure the viscosity of actively flowing lava *in situ*, using data from a rotational viscometer (see Chevrel et al. 2018). Other than these few *in situ* measurements, the body of research on active flow rheology has relied heavily on calculations using remote sensing data.

Three of the most common remote sensing techniques used for collecting data on active lava flows in the field are photogrammetry (for modelling 3-dimensional morphology), digital video recording (for velocimetry), and thermal infrared imaging (for measuring surface temperature). Photogrammetry has become widely used in the past decade in volcanology due to its ability to produce low-cost, high-accuracy 3D models of lava flow surfaces (James and Robson 2012). However, using this technique on a moving target, such as an active lava flow, is much more difficult and has only been attempted a few times (Dietterich et al. 2015; Farquharson et al. 2015; Hamilton et al. 2013; James and Robson 2014; James et al. 2007). Similarly, velocimetry of lava flows via analysis of video data has proven a challenging task, although this challenge has been overcome recently by the integration of recording devices with unmanned aerial systems (drones) in volcanological research. One of the earliest attempts of video-based lava velocimetry was by Sakimoto and Gregg (2001). They showed that the velocity of a lava channel could be estimated by the tracking of prominent floating features. Further research on lava velocimetry employed the optical flow method (Horn and Schunck 1981; Lucas and Kanade 1981), which can be used to generate a velocity field given sequential images or video frames (Dietterich et al. 2015; James et al. 2012; James et al. 2007; Lev et al. 2012; Rumpf et al. 2018; Walter 2011).

Thermal infrared imaging, in contrast to visible light imaging techniques, is likely one of the most common volcano monitoring methods, with satellite applications dating back to the 1960s and handheld applications gaining popularity in the early 2000s (Harris et al. 2005; Wright et al. 2004). Long-range applications (> 10 m) have proven successful in identifying relative temperature anomalies and imaging lava flows whereas short range applications are useful for mapping absolute temperatures on lava surfaces (e.g., Harris et al. 2005; Lev et al. 2012; Patrick et al. 2007).

The goal of this study is to apply these well-established techniques of photogrammetry, velocimetry, and thermal infrared imaging in tandem to solve for the temporal and spatial viscosity field of an experimental lava flow, using available analytical models. Because these data collection methods are already prevalent in field volcanology, the new technique of *viscosity mapping* described below should be applicable to certain natural settings. Such applications would greatly advance our understanding of the rheology of actively flowing lava.

Methods

Experimental lava flow

The experimental lava flow in this study was a product of the Syracuse Lava Project in Syracuse, NY (http://lavaproject.syr.edu/). The Syracuse Lava Project has been utilized as a laboratory to study the rheology and emplacement mechanisms of basaltic lava flows by many researchers (Cordonnier et al. 2016; Dietterich et al. 2015; Dietterich et al. 2017; Edwards et al. 2013; Farrell et al. 2018; Lev et al. 2012; Rumpf et

al. 2018). These controlled, large-scale experiments can be used as a testing environment for instrumentation applications and techniques to be deployed in natural settings. At this facility, a gas-fired tilt-furnace was utilized to melt basaltic rock to super-liquidus temperatures (>1300° C) and generate a meter-scale, glassy, lava flow. The lava flow analyzed in this study was emplaced on a groomed coarse sand substrate (dry to atmospheric conditions) with a 10° slope (Figure 1). This lava flow was chosen as a case study for viscosity mapping because of its simple sheet-like shape, vesicle- and crystal-limited melt phase, and high-quality photogrammetric and thermal infrared data coverage. The bulk major element chemistry of this lava flow characterizes it as basaltic andesite in composition (SiO_2 ≈ 53%) with no measurable volatiles (LOI ≈ 0) (Table 1).

In the tilt furnace experiment, the lava was poured from a silicon carbide crucible onto a steel trough that guided the lava on to a gently inclined surface (Figure 1). The lava exhibited sheet-like behavior (maintaining approximately constant thickness) throughout the flow with no visible inflation effects. An outer viscoelastic crust was assumed to cover the lava flow during the data collection interval, based on surface temperatures measurements below the viscoelastic transition for basalt (1050° C) (Hon et al. 1994) (Figure 2). At about t = 40 s, small-scale folds (1–2 cm wavelength) appeared on the lava surface, further suggesting the presence of a viscoelastic crust (Figure 1) (Farrell et al. 2018; Fink and Fletcher 1978). Throughout the experiment and until the flow came to rest, the inferred layered structure of the flow was a continuous, thin viscoelastic crust above a viscous core (Figure 2). This crust likely thickened via cooling after the lava supply was cutoff around t = 60 s. A brittle crust, defined by surface temperatures below the glass transition, did not develop until after the data

collection interval (Table 2). The glass transition temperature of this material is about 660° C (Sehlke and Whittington 2016).

The experiment lasted about 160 seconds, which represents the time between initial substrate contact and flow arrest. Photogrammetric and FLIR infrared data coverage spanned a time interval between t = 12 s and t = 82 s. Internal temperature of the lava was measured with a type K thermocouple inserted directly into the flow. The thermocouple was inserted late in the experiment, at about t = 60 s, so that the perturbation would not significantly affect the flow behavior or morphology, and thus, viscosity calculations. The thermocouple reach equilibration by t = 98 s and at this time recorded an internal temperature of 1230°C.

Time-lapse photogrammetry

Time-lapse 3D models of the lava flow were created using a custom-built photogrammetric imaging device. The apparatus consists of 10 digital cameras (Canon SX530) mounted on an arcuate, 2 m wide steel frame that situated 3 m above the flow during the experiment (Figure 3). The cameras are each spaced approximately 20 cm apart on the frame and each one focused on the sloped substrate. Each camera was equipped with open-source software used for synchronous USB triggering (CHDK or Canon Hack Development Kit) installed on the memory cards. This allowed for user-controlled activation of the shutters on all 10 cameras by applying a small voltage to the USB port. The cameras were linked to a powered 5V, 3.5A USB hub via 1 m cables and the USB hub was attached to a user-controlled power switch. Activating the power

switch signaled all cameras to engage simultaneously, thus capturing 10 synchronous images of the lava flow from different angles. The on/off power cycle of the USB hub allowed for capturing of an image set about every 7-10 seconds.

After the experiment, the digital photographs were exported and prepared for photogrammetric processing. The images were sorted into subsets, each with a time stamp derived from the JPEG meta data. Image subsets were processed using the Structure-from-Motion photogrammetry method, executed in Agisoft Photoscan (see James and Robson (2012)). This process yielded one high-resolution 3D point cloud per time step. The 3D point clouds were transformed into orthorectified digital terrain models (DTMs) using linear scale bars on the substrate slope. The DTMs were initially bound by an arbitrary elevation datum, but by using the lava-free substrate slope DTM (i.e. t = 0 s) as the initial condition, the lava surface elevation was converted to lava thickness for each model using raster calculations, executed in qGIS. By subtracting the lava DTMs from the substrate DTM, each pixel was transformed from a relative elevation to a thickness (Figure 4).

In addition to mapping lava flow thickness, this method was also used to derive a high-resolution substrate slope map for the experiment. For typical experimental purposes, assuming a perfectly planar slope can be justified, but the high-resolution photogrammetry allowed for a more detailed treatment of the slope parameter. Micro-topography of the substrate, dominated mostly by the roughness of the sand, was transformed into a high-resolution DTM. From this topography, a slope map was calculated using the slope analysis tool in qGIS. This step may prove useful in natural settings, where substrate topography can be more complex.

Similar time-lapse photogrammetry methods have been used in experimental settings (Dietterich et al., 2015) and in the field during active eruptions (James and Varley, 2012; Hamilton et al., 2013; Farquharson and Tuffen, 2015) to quantify lava flow emplacement and behavior at various scales. No study, however, has used this method to map the apparent viscosity field of an active lava flow through time.

Velocimetry

Lava flow surface velocity was calculated using digital particle image velocimetry, executed in the Matlab toolbox PIVlab (Thielicke and Stamhuis 2014). This toolbox applied particle tracking algorithms to pixels of consecutive digital video frames to create vector velocity fields. This technique was applied using vertical video from the lava flow experiment with extracted frames synchronous with the DTM frames. Using the extracted velocity vector fields, the absolute magnitudes of velocity were calculated and averaged over five consecutive frames spanning the desired time step. This yielded one velocity magnitude field per time step with a spatial resolution of 1 cm^2 (Figure 4). The velocity fields were georeferenced using qGIS to overlay precisely on the corresponding DTMs. PIVlab and other similar particle tracking methods have been used successfully in volcanological studies for velocimetry of lava flows (e.g. Lev et al., 2012; Slatcher et al., 2015; Rumpf et al., 2018) and analog models of pyroclastic density currents (Breard et al. 2016; Lube et al. 2015).

Thermal infrared imaging

Thermal imagery was captured using a FLIR T300, capable of recording mid-infrared (7.5 to 13μm) data at a resolution of 320x240 pixels and 30 Hz frame rate. The FLIR camera was positioned on the same platform as the photogrammetry apparatus, about 3 meters from the lava flow surface (Figure 2). An emissivity value of 0.93 was used in this experiment, following Lev et al. (2012). From the FLIR video of the experiment, individual still images were extracted that match the time steps used in the photogrammetry and velocimetry procedure, synchronized via audio queues in the FLIR recording. The extracted thermal images were georeferenced and scaled to match the lava thickness DTMs and velocity maps. This was achieved using point-based georeferencing, executed in qGIS (Figure 4).

Viscosity mapping

To create time-lapse viscosity maps of the active lava flow, two viscosity models were applied that are commonly used in field and experimental volcanology. The first model applied was the Jeffreys equation (Jeffreys 1925) for viscous, non-channelized flow:

$$\eta_a = \rho g h^2 sin\theta / 3V \quad (1)$$

In this equation, V is surface velocity, ρ is density, g is gravity, h is lava thickness, θ is substrate slope, and η_a is the apparent viscosity. As previously discussed, apparent viscosity is a depth-averaged value generalizing the heterogenous rheology of the flow.

For this experiment, the assumed layered structure of the lava flow consisted of a thin viscoelastic crust (η_o) and a viscous core (η_i) (Figure 2). If the values of h and V used in the Jeffreys equation are not substantially influenced by the presence of a viscoelastic crust, then apparent viscosity approximates core viscosity:

$$\eta_a \cong \eta_i \quad (2)$$

The inherent assumption of Newtonian flow in the Jeffreys equation may not always be consistent with multi-phase fluids (e.g. lava + crust + bubbles), but it can be a useful calculation for comparative rheology between lava flows. It also has proven to be a favorable model used in conjunction with the imaging method presented here because most of the parameters (i.e. h, V, θ) were calculated over space and time and thus, apparent viscosity can be presented as time-series maps instead of a single scalar value.

To execute this viscosity model, the thickness and slope DTMs were down-sampled to 1 cm^2 resolution to match the velocimetry rasters. Once the raster resolutions were synchronized, the Jeffreys equation was solved at each pixel using raster calculations, executed in qGIS. Gravity and density were both assumed constant in this model at 9.8 m/s^2 and 2700 g/cm^3, respectively, following Lev et al. (2012). Repeating this process for each time-step resulted in 10 apparent viscosity maps of the lava flow as it evolved through time.

The other viscometry approach applied to this problem was the GRD model (Giordano et al. 2008). GRD is a multicomponent chemical model used to predict temperature-viscosity curves for silicate melts. Unlike the Jeffreys equation, this

required parameter inputs of bulk chemical composition of the lava and temperature. To determine melt viscosity from temperature values, the GRD viscosity curve for Syracuse Lava (Table 1) was fit with an exponential function:

$$\log \eta = 102.835 \mathrm{e}^{-0.003T} \qquad (3)$$

In this equation, η is the melt viscosity and T is the temperature. As previously discussed, melt viscosity is the predicted homogenous fluid viscosity and is applicable for viscous and viscoelastic materials. The exponential regression across the working range of temperatures (700 - 1200 °C) yielded an R^2 value above 0.99 (Figure 5).

Because this lava flow exhibited a thin viscoelastic crust during the experiment, the surface and interior temperature values were treated separately. The surface temperatures, measured with FLIR infrared imagery, are assumed to represent the crust and the interior temperatures, measured with a thermocouple, are assumed to represent the core (Figure 2). Therefore, calculated melt viscosity values using surface temperatures and the GRD model were assumed to represent the crustal rheology:

$$\eta_1 = \eta_o \quad (4)$$

And melt viscosity values using the thermocouple temperatures were assumed to represent the core rheology:

$$\eta_2 = \eta_i \quad (5)$$

Results

Velocity, thickness, and surface temperature

Using the described methods, ten time-series rasters were generated containing velocity, thickness, and surface temperature data, and one initial condition raster containing slope data. The first time-step (t = 12 s) raster contained N = 688 individual data points (1 cm^2 pixels) and this N value increased as the lava flow grew in size to a final value of N = 4398 data points at t = 82 s (Table 2). In total, there were 26,840 individual measurements of velocity, thickness, and surface temperature.

Mean velocity values of the lava flow surface ranged from 0.4 to 1.5 cm/s. Flow velocities were mostly stable around 1.5 cm/s until t = 49 s after which mean velocity values steadily decreased to a minimum of 0.4 cm/s at t = 82 s. Standard deviations of mean velocity were typically about 0.5 cm/s (Table 2).

Mean thickness values of the lava flow ranged from 1.9 to 2.6 cm. The lava flow maintained a nearly constant thickness throughout the experiment with a time-averaged mean value of 2.3 ± 0.2 cm.

Mean surface temperature values of the lava flow ranged from 889° to 1019°C. These mean values decreased steadily throughout the experiment whereas the standard deviation steadily increased from 47° to 91°C. The lowest temperature values were always observed on the margins of the flow and the highest values in the flow center.

Slope of the planar substrate was measured at 10° with a clinometer in a central location on the steel plane. As previously described, slope was also calculated using a

DTM of the substrate plane. Mean slope value calculated using photogrammetric DTMs was 9.5° ± 2.8°. The slope raster values were used in calculations of apparent viscosity.

Jeffreys equation results

Apparent viscosity (η_a) maps derived using the Jeffreys equation were generated as a time-series and presented in Figure 6. As previously described, these values are likely a close approximation of the melt viscosity of the lava core (η_i) (Equation 2). Over the 82 seconds of data collection in the experiment, mean apparent viscosity values ranged from log 1.4 to log 2.1 (Pa s) (Table 2). After t = 41 s, a spatial pattern developed wherein low viscosity values clustered towards the interior of the flow and high viscosity values concentrated along the outer margins of the flow. This pattern can be seen in time steps 49 s through 82 s (Figure 6). The apparent viscosity values were within the range of previous viscometry studies of Syracuse Lava (Farrell et al. 2018; Lev et al. 2012).

GRD results

Melt viscosity maps derived using the GRD method and FLIR infrared temperature values were generated as a time-series and presented in Figure 7. As previously described, these values are assumed to represent the melt viscosity of the lava crust (η_o) (Equation 4). Over the course of the experiment, mean melt viscosity values for the crust ranged from log 4.4 to log 6.3 (Pa s) (Table 2). Similar to the

apparent viscosity results above, a spatial pattern developed wherein low melt viscosity values clustered towards the interior of the flow and high melt viscosity values concentrated along the outer margins of the flow. Melt viscosity values for the crust were, on average, five orders of magnitude higher than the apparent viscosity values derived using the Jeffreys (1925) equation (Table 2).

The GRD method was also applied to derive melt viscosity based on thermocouple temperatures, which are from the lava core. As previously described, the thermocouple was inserted around t = 60 s and equilibrated by t = 98 s, recording a maximum temperature of 1230° C. The melt viscosity for the lava core derived using GRD (Equation 3) for this maximum temperature is log 2.2 (Pa s). Three subsequently recorded temperature values at t = 108 s, 118 s, and 128 s were also converted to melt viscosity using GRD and are presented in Figure 8. These values are assumed to represent the melt viscosity of the lava core (η_i) and, although they are not contemporaneous, do closely match the apparent viscosity values (η_a) calculated using the Jeffreys equation described above (Figure 8).

Discussion

The results of this experiment have revealed, for the first time, the detailed time-series viscosity field of a lava flow, with implications for layered rheology. This was achieved using only digital cameras, a FLIR thermal infrared device, and the analytical models of Jeffreys (1925) and Giordano et al. (2008). Below is a discussion of these

results and interpretations of the spatial viscosity patterns, implications for solving layered rheology, and future applications for natural lava flows.

Spatial viscosity patterns

One of the most prominent features revealed in the time-series viscosity maps was the spatial division of high and low values. In both models, the low viscosity values tended to cluster near the center of the flow and the high viscosity values appeared on the flow margins (Figures 6 and 7). Although this pattern was anticipated qualitatively based on known flow behaviors, it has never been addressed quantitatively. The observed pattern of progressively solidifying flow margins suggests the development of incipient levees. Levees in natural lavas develop as the margins of a lava flow cool and solidify at a higher rate than the flow core, channelizing the flow (Hulme 1974; Sparks et al. 1976). In this experimental lava flow, the incipient levees of high viscosity lava appeared around t = 49 s and continued to propagate downslope and eventually towards the center as the lava supply was cutoff. In the apparent viscosity maps (Jeffreys equation, Figure 6), viscosities along the margin increased mainly due to lateral velocity gradients. Velocities near the margins were consistently lower after about t = 41 s (e.g. Figure 4). In the melt viscosity maps of the crust (GRD, Figure 7), the high viscosities along the margins were a result of lower surface temperatures. Although the two viscosity datasets agree on relative patterns, the absolute magnitudes are vastly different. In the final data series time step, t = 82 s, the apparent viscosities were around log 3.0 (Pa s) near the margins and the melt viscosities of the crust were around log 10.0 (Pa s) near the margins.

This observation of incipient levee development represents a transition between sheet flow behavior and channelized behavior (Kerr et al. 2006). This transition has been well-documented in wax (polyethylene glycol) analog studies (Gregg and Fink 2000; Hallworth et al. 1986; Kerr et al. 2006), but is less well-understood in natural lava flows (Sakimoto and Gregg 2001). In this lava experiment, had the lava output rate continued steadily, fully solidified levees would have developed, and open channel flow would have likely been the dominant mode of transport. This is commonly observed in Syracuse Lava experiments. Channelized behavior has been documented in higher volume lava flow experiments at similar slopes (≥10°) (Lev et al. 2012).

Understanding the development of levees with respect to viscosity gradients has broad implications for modelling channelized lava flow behavior. Lava channels are a common emplacement feature and can facilitate the transport of molten material over significant distances compared to other modes of flow (Harris and Rowland 2009; Walker 2009; Walker 1991). More experiments are needed to fully quantify the relationship between rheology and levee development, but this experiment illustrates the feasibility of such an investigation in experimental lava.

Solving for layered rheology

As previously discussed, the significant disparity in orders of magnitude between the two viscosity solutions is likely due to the presence of a viscoelastic crust on the lava flow (Figure 2, Figure 8). The presence of a viscoelastic crust, however, does not imply any that the overall behavior of the flow was influenced by the crust. In other words, a lava flow can initially have a viscoelastic crust of high viscosity, but that crust

may have insufficient thickness as to influence the dynamics (specifically, velocity and total thickness) of the flow. If the crust is so thin (< 1 mm) that it does not significantly contribute to the total thickness (h) or inhibit the velocity (V) of the molten core, then the solution to the Jeffreys equation (η_a) should closely match the true melt viscosity of the core (η_i).

To test this assumption, the melt viscosity of the core was calculated independently using the temperatures measured by the type K thermocouple that was inserted into the interior of the lava flow. As previously discussed, the thermocouple was inserted around t = 60 s and registered a maximum temperature of 1230° C at t = 98 s. Using the GRD model (Equation 3), a core temperature of 1230°C corresponds to a melt viscosity of log 2.2 (Pa s). The Jeffreys equation solved at the final time step (t = 82 s) yielded a mean apparent viscosity of log 2.1 ± 0.3 (Pa s) (Figure 8). Although the two results are not contemporaneous (separated by ~14 s), the general agreement between the two solutions suggests that the Jeffreys equation is indeed a very close approximation of the melt viscosity of the core (η_i), given a lava flow with a viscoelastic crust of insignificant thickness. More experiments with improved thermocouple core temperature coverage will help further test this assumption.

One of the important implications of this observation is in evaluating the crust-core viscosity ratio (η_o:η_i) (Figure 2). This ratio, termed R in some studies, is a factor that exhibits a strong control on flow morphology, specifically with respect to surface folding (Farrell et al. 2018; Fink 1980; Fink and Fletcher 1978; Gregg et al. 1998). Surface folding, the process responsible for ropy-pāhoehoe texture, is a typical morphology at high viscosity ratios ($R > 10^2$) (Biot 1961; Fink and Fletcher 1978). For

this lava experiment, the R value is remarkably consistent throughout the data collection interval at around 10^5, a high value that would predict folding (Table 2). As seen in Figure 1, the dominant surface morphology can be described as folded, thus, the viscosity ratio is consistent with observed morphology. Although this is only one observation, future experiments may reveal a quantitative relationship, or even a predictive model, between viscosity ratios and flow morphology.

Field applications

The method described in this study for mapping lava flow viscosity was applied in a large-scale experimental setting but may prove practical in certain active flow fields. As previously discussed, the three primary modes of data collection, time-lapse photogrammetry, video-based velocimetry, and thermal infrared imaging, have all been successfully used to monitor active eruptions and characterize lava flows. The most sensible application of this integrated method would likely be at an advancing pāhoehoe flow field, where conditions can be favorable for collecting such data. For example, Hamilton et al. (2013) successfully generated time-series DTMs of an advancing pāhoehoe lava flow at Kilauea Volcano using ground-based repeat photogrammetry and differential GPS methods. Attempting a viscometry study in a similar scenario would need only the addition of one unmanned aerial vehicle equipped with either a multispectral camera or simply a thermal infrared camera capable of vertical video recording. This would allow for the total suite of data acquisition techniques required for viscosity mapping.

In less accessible volcanic environments, this technique could be applied using only unmanned aerial vehicles. In principle, photogrammetric modelling requires photographs from only two angles (stereophotogrammetry) to generate a 3D model (e.g. James and Robson, 2012). Integrating vertical multispectral video (for velocimetry and thermal analysis) with stereophotogrammetry would only require three unmanned aerial vehicles. This would allow for 4-dimensonal viscometry at a variety of scales and locations. Future testing of this design across solidified lava fields would be useful to determine feasibility for deployment in active eruption scenarios.

Conclusions

Combining remote data acquisition techniques such as time-lapse photogrammetry, thermal infrared imaging, and vertical digital video allows for solving the 4-dimensional viscosity field of a lava flow. For large-scale experimental lava flows with thin, viscoelastic crusts, the melt viscosity of the molten core can be approximated using the Jeffreys equation and the melt viscosity of the crust can be calculated using surface temperatures and the GRD model (Giordano et al. 2008). Results of this experiment also revealed the rheologic framework for the incipient development of levees, thus capturing a critical transition between sheet and channelized behavior. Although the techniques in this study have been applied in the laboratory, the data acquisition methods are commonly used in field volcanology. Applying this workflow in natural settings to evaluate active flow viscosity will greatly expand our understanding of lava rheology and behavior.

Tables

Table 1. Normalized major element compositions in weight percent for the experimental lava used in this study. Geochemical analyses were performed using wavelength dispersive spectroscopy on pure glass samples at the Syracuse Microprobe Laboratory.

Syracuse Lava	SiO_2	TiO_2	Al_2O_3	FeO	Na_2O	MgO	K_2O	CaO	MnO	P_2O_5	Cr_2O_3	Total
x̄	**53.18**	**1.89**	**14.64**	**11.27**	**1.97**	**6.09**	**0.89**	**9.72**	**0.18**	**0.18**	**0.01**	**100.00**
+/-	**0.13**	**0.02**	**0.06**	**0.15**	**0.05**	**0.03**	**0.02**	**0.08**	**0.03**	**0.02**	**0.02**	**-**

Table 2. Results from the described viscosity modelling workflow. All symbols are described in the text.

Time (s)	N	V (m/s)	1σ	h (m)	1σ	T (°C)	1σ	Log η_a (Pa s)	1σ	Log η (Pa s)	1σ	R	log R
12	688	0.015	0.005	0.019	0.006	1019	47	1.5	0.3	4.4	0.7	47164	4.7
20	1155	0.017	0.007	0.020	0.007	988	54	1.4	0.3	4.7	0.8	181844	5.3
27	1631	0.015	0.007	0.023	0.007	961	60	1.6	0.2	5.1	1.0	108268	5.0
34	2080	0.015	0.006	0.025	0.006	956	75	1.7	0.2	5.3	1.2	86750	4.9
41	2544	0.014	0.005	0.026	0.006	959	86	1.8	0.2	5.3	1.5	48982	4.7
49	3037	0.012	0.007	0.024	0.006	948	82	1.8	0.2	5.4	1.4	59049	4.8
56	3437	0.011	0.006	0.026	0.006	946	82	1.9	0.2	5.5	1.4	41313	4.6
63	3746	0.008	0.005	0.024	0.005	926	89	2.0	0.3	5.7	1.6	35355	4.5
73	4121	0.006	0.004	0.023	0.004	913	86	2.0	0.3	6.1	1.5	69662	4.8
82	4398	0.004	0.003	0.021	0.004	889	91	2.1	0.3	6.3	1.8	59049	4.8
x̄	2684	0.012	0.005	0.023	0.006	951	75	1.8	0.3	5.4	1.3	73744	4.8
1σ	1275	0.004	0.001	0.002	0.001	37	16	0.2	0.1	0.6	0.4	43894	0.2

Figures

Figure 1. Time-lapse imagery of the experimental basaltic lava flow used in this study. Scale bar divisions – 10 cm.

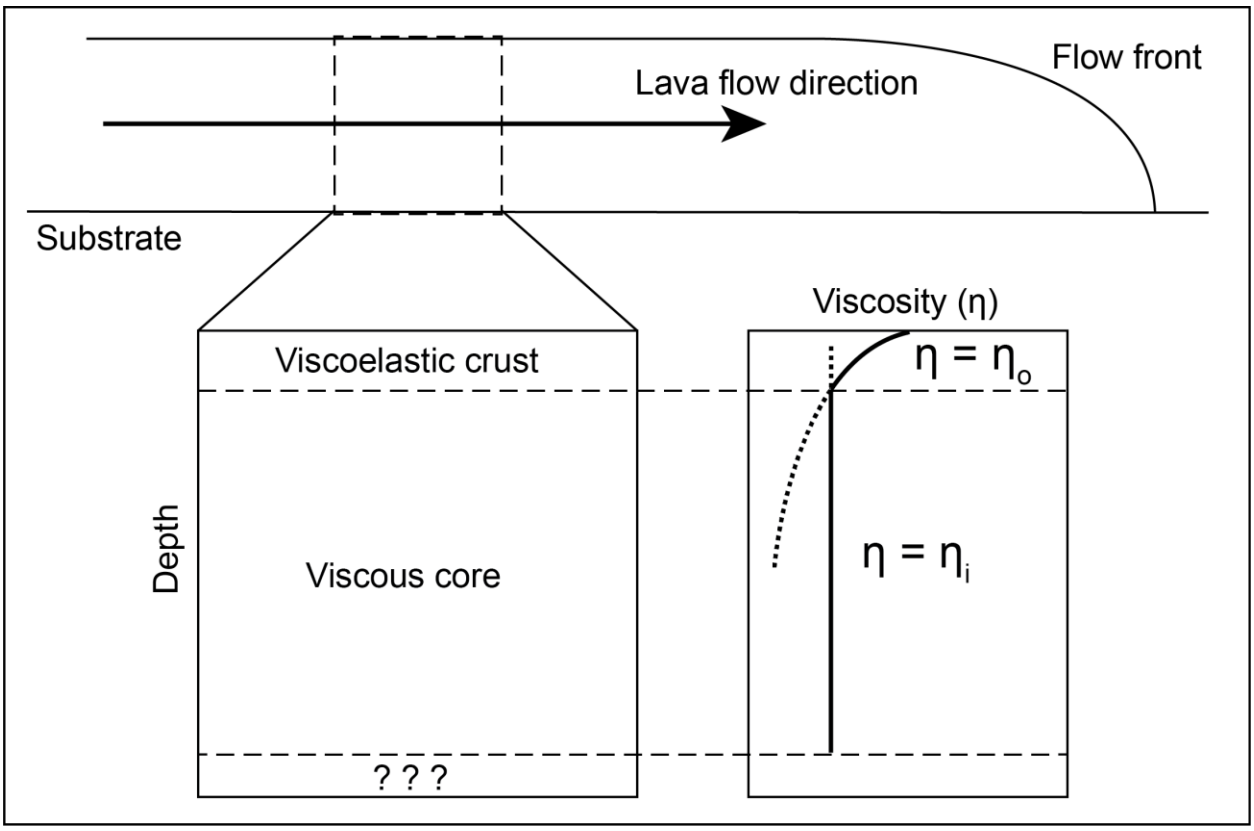

Figure 2. Cross-sectional schematic with viscosity profile interpretation for the lava flow experiment. η_o – outer (or crust) viscosity; η_i – inner (or core) viscosity. Viscosity profile modified from Fink and Fletcher (1978). Thickness of viscoelastic crust greatly exaggerated.

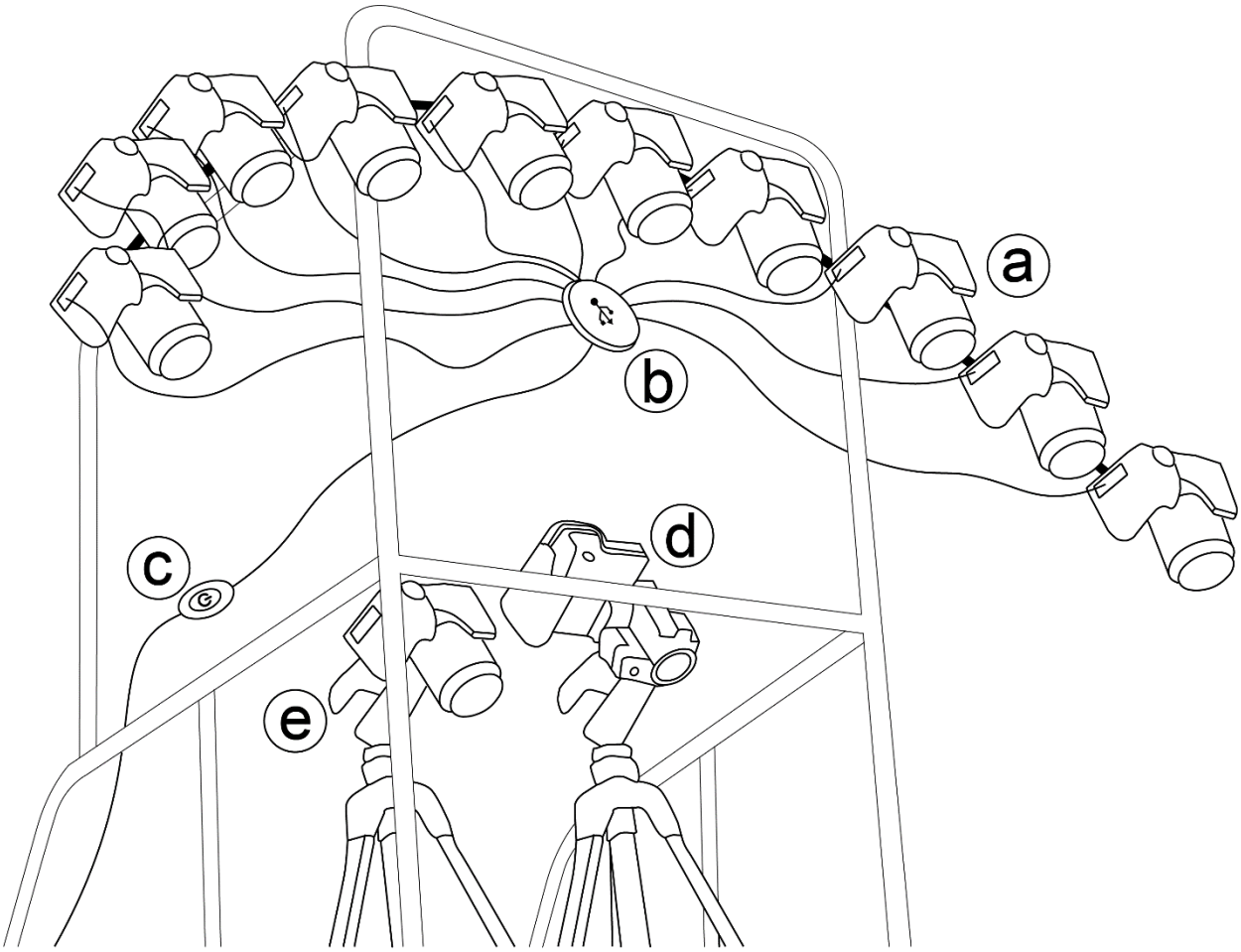

Figure 3. Data collection apparatus used during lava flow experiments. A – time-lapse photogrammetry array. B – USB hub. C – User-operated power switch for activating USB hub. D – FLIR t300 thermal infrared camera. E – Digital SLR camera for video recording.

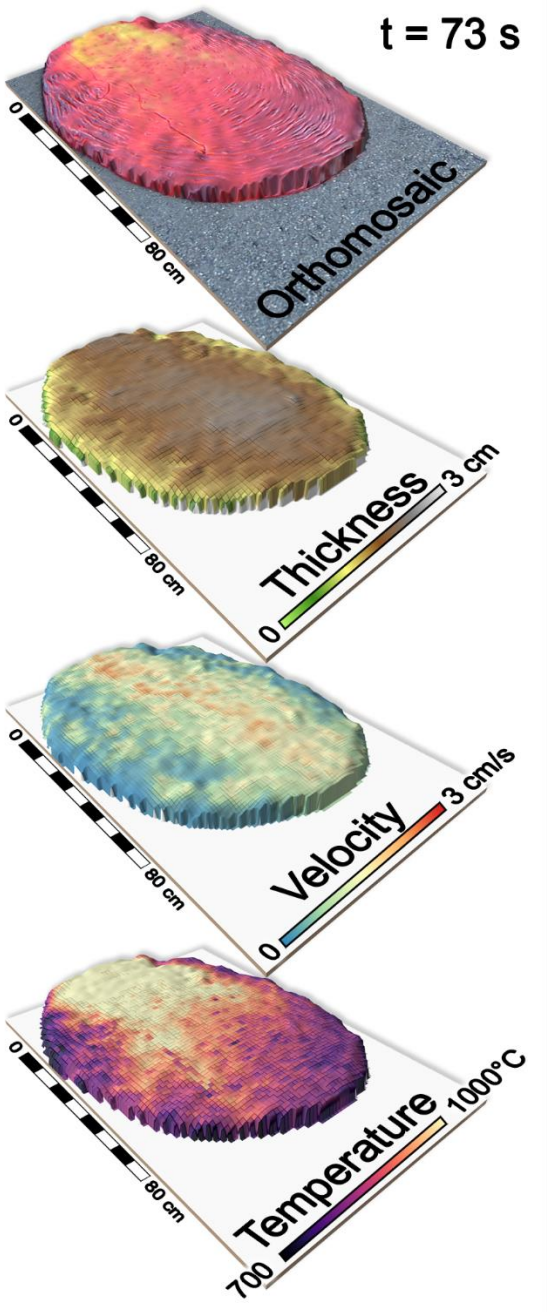

Figure 4. Oblique view of digital raster data for the experimental lava flow at time step t = 73 seconds. Rasters are draped over a photogrammetric 3D model of the flow. Vertical exaggeration – 2x.

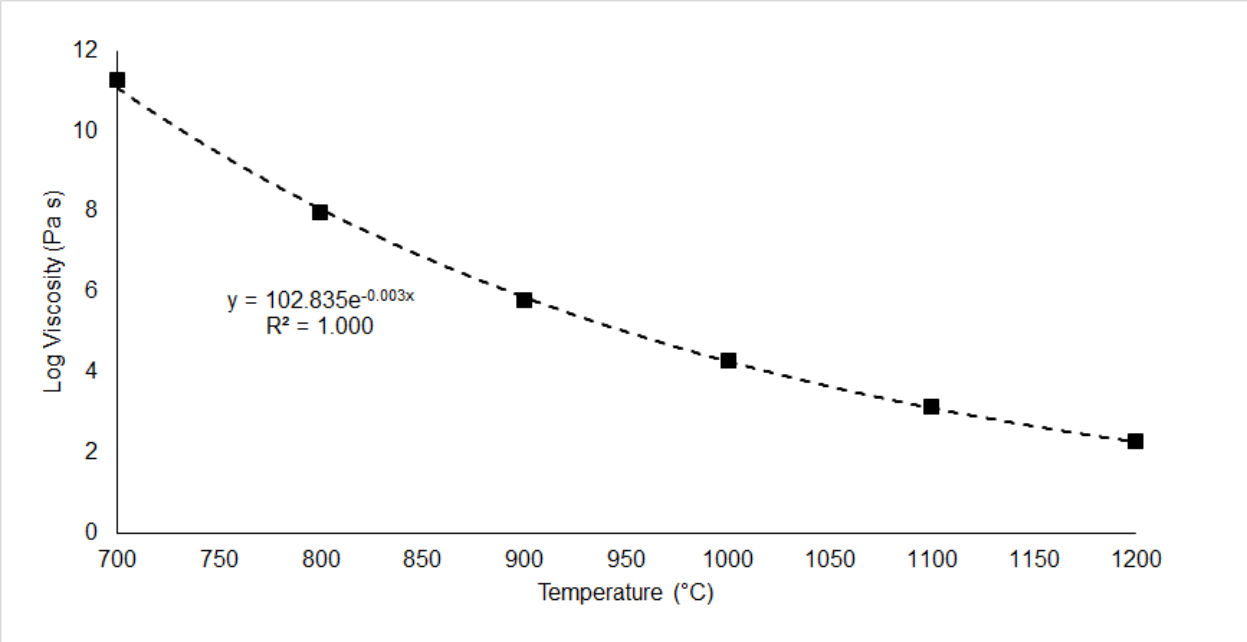

Figure 5. Viscosity-temperature curve for the experimental lava flow. Black boxes – viscosity values calculated using the GRD model. Dotted line – exponential regression of data.

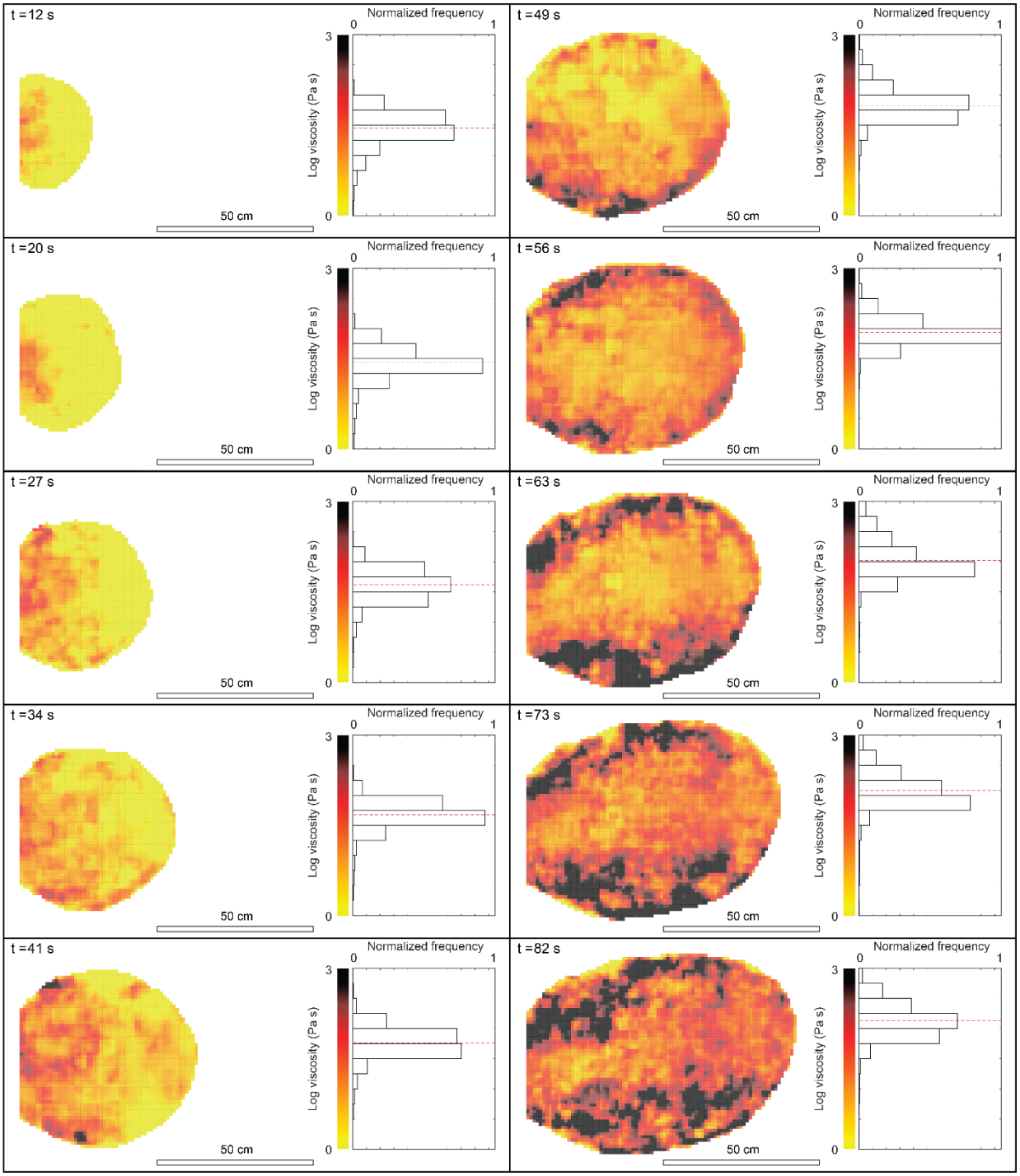

Figure 6. Time-lapse apparent viscosity maps and histograms of the experimental lava flow calculated using the Jeffreys equation.

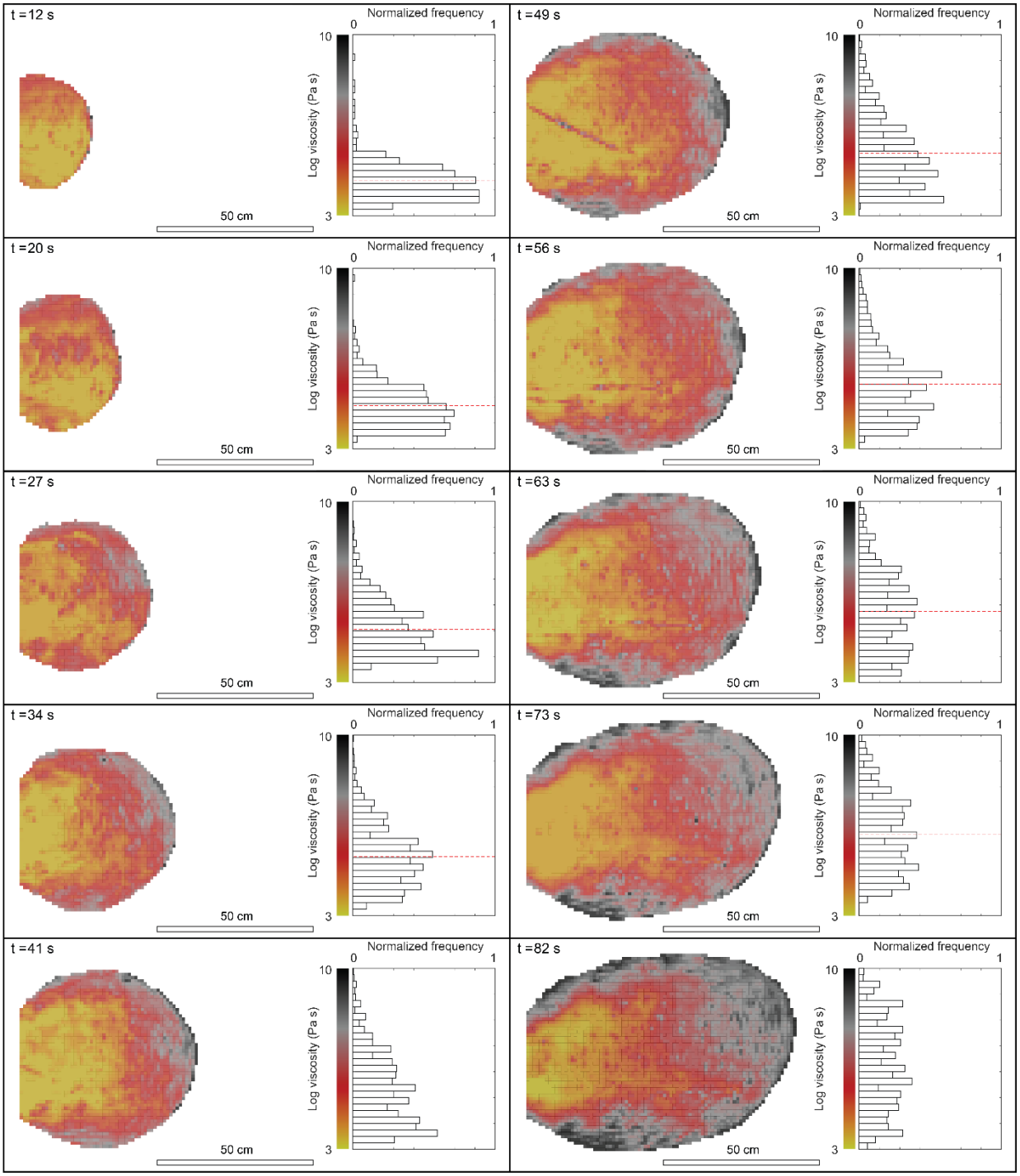

Figure 7. Time-lapse melt viscosity maps and histograms of the experimental lava flow calculated using the GRD model.

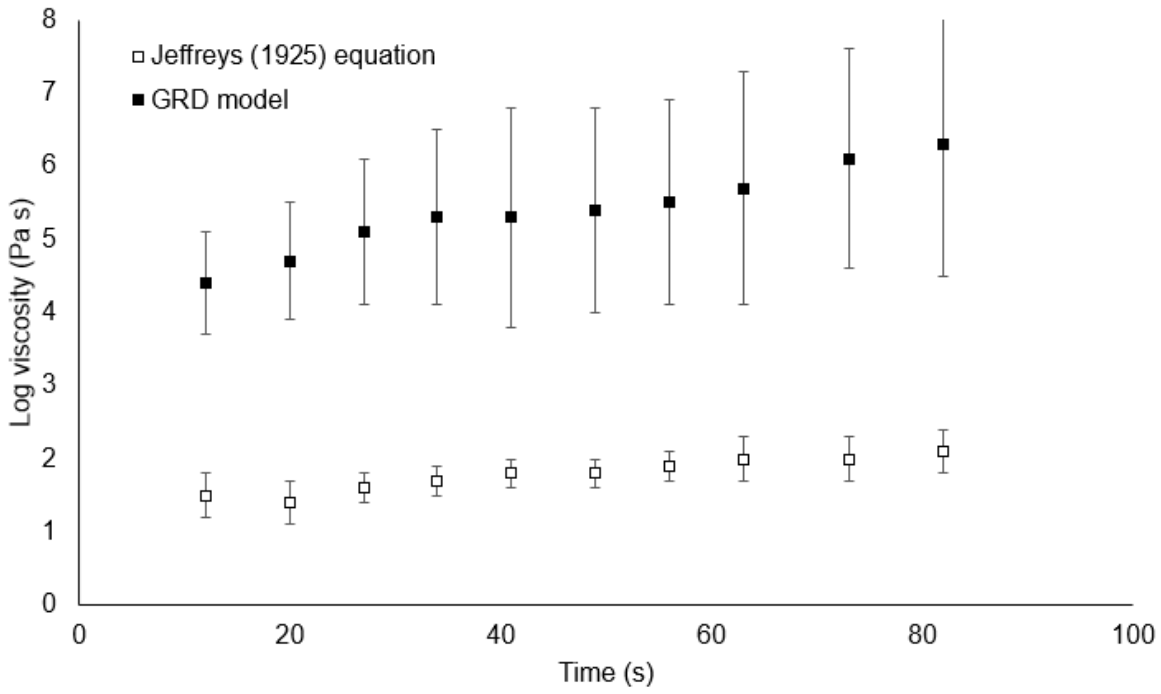

Figure 8. Mean values of lava viscosity over time calculated using the described models. Error bars – 1σ.

Chapter 3: Predicting the locations of breakouts in basaltic lava flow experiments

In preparation for submission to:

Geology

Abstract

Inflation and breakout are two fundamental mechanisms involved in the emplacement of basaltic pāhoehoe lava flows, the most common lava flow type on Earth and other planetary surfaces. Breakouts occur when the fluid pressure within the molten core of a lava flow lobe exceeds the yield strength of the surrounding crust. This can occur during failure (fracturing) of the exterior brittle crust, hyperextension of the viscoelastic crust, or a combination of the two, depending on the flow structure. Therefore, a relationship should exist between the loci of lava breakouts and the relative position of greatest internal pressure and/or weakest overlying crust. We tested this hypothesis with detailed observations of meter-scale experimental basaltic lava lobes. Breakout locations for seven lava lobes were predicted within about 10° of angular uncertainty by using surface temperature patterns to identify weaknesses in the crust and thickness patterns to identify locations of high internal pressure. Furthermore, we identified two end-member cases for lobe development wherein rheological weaknesses are either correlated or uncorrelated to locations of high internal pressure. This suggests a complex balance between deterministic and probabilistic factors influencing the location of lava flow breakouts.

Introduction

Basaltic pāhoehoe lava flows represent a dominant surface feature on Earth and other terrestrial planets (e.g. Self et al. 1998). These types of lava flows tend to be laterally extensive, but are commonly constructed from individual meter-scale lobes that advance and coalesce over time to form flows and flow-fields (e.g. Crown and Baloga 1999; Hoblitt et al. 2012; Hon et al. 1994). This mechanism of coalescence can create a network of thermally insulated fluid pathways that enable the transport molten lava over long distances and with very low cooling rates (Harris and Rowland 2009; Walker 2009; Walker 1991). It has even been suggested that these processes associated with pāhoehoe flow development are influential in the construction of some continental flood basalts (Kent et al. 1998; Self et al. 1997; Thordarson and Self 1998; Vye-Brown et al. 2013). Although these broad-scale volcanic processes depend on the behavior of individual lobes, relatively little attention has been given to the mechanics of these structures.

Of the lava flow observations that have been made at the centimeter- to meter-scale, it has been shown that two of the fundamental mechanisms affecting pāhoehoe lobe behavior are inflation and breakouts (Crown and Baloga 1999; Hamilton et al. 2013; Hoblitt et al. 2012; Hon et al. 1994). Lava inflation occurs due to initially rapid thickening of the molten core and gradual thickening of the viscoelastic and brittle crust layers (Cashman et al. 1999; Hon et al. 1994). Breakouts occur when the internal viscous fluid pressurizes and escapes through weaknesses in the crustal layers, leading to the development of a new lobe (Crown and Baloga 1999; Hoblitt et al. 2012; Hon et

al. 1994). Studies have shown that this process is highly sensitive to stochastic influences and can be approached with probabilistic models (Glaze and Baloga 2013; Glaze and Baloga 2016; Hamilton et al. 2013; Kilburn 1996). Lava breakout location is one of many stochastic parameters in lava flow models and is commonly handled with a combination of probabilistic and deterministic constraints (Baloga and Glaze 2003; Glaze and Baloga 2013; Hamilton et al. 2013; Kilburn 1996).

The aim of this study is to assess the influences of breakout location in meter-scale experimental lava flows using time-series observations of thickness and surface temperature patterns. Understanding the both the deterministic and probabilistic nature of inflation and breakout at this scale has implications for modelling not only lava lobes, but the emplacement of entire flow-fields (Bruno et al. 1994; Glaze and Baloga 2013; Glaze and Baloga 2016; Hamilton et al. 2013). Furthermore, meter-scale processes provide crucial information for assessing potential flow trajectories and related hazards and interpreting the morphology of solidified flows (Byrnes and Crown 2001; Gregg 2017; Peitersen and Crown 2000).

Methods

Seven basaltic lava flow experiments were conducted at the Syracuse Lava Project using a high-volume, gas-fired tilt furnace capable of melting rock at super liquidus temperatures (>1400° C) (http://lavaproject.syr.edu). The lava flows were emplaced on a groomed, planar sand substrate with slopes between 5° and 10°. Each lava flow evolved with a similar three-stage emplacement pattern: sheet-like viscous gravitational spreading, followed by stalling and inflation, and eventual breakout. The

inferred rheological structure of these lobes is consistent with natural lavas wherein a viscous core is overlain by a viscoelastic crust and an outermost brittle crust. (Hon et al. 1994). Breakouts in experimental lobes occurred by hyperextension of the viscoelastic layer, commonly after the layer was exposed by pressure-driven uplift of the brittle crust. No breakouts exploited the brittle crust directly.

The time between stall of lateral spreading and breakout for a given lobe was on the order of tens of seconds and as high as three minutes. Individual lobes measured 85 ± 32 cm in length and 64 ± 13 cm in width (all uncertainties reported in this study are 1σ unless otherwise noted). Average output rates of lava flows at this facility were calculated in a previous study and were on the order of 2×10^2 cm^3/s (2×10^{-4} m^3/s) (Farrell et al. 2018). All flows examined were aphyric to crystal-free glass and predominantly exhibited single phase behavior, although some vesicularity (< 15%) was observed in isolated samples.

Evolution of lava flow thickness and surface temperature was documented using a custom time-lapse photogrammetry apparatus and a thermal infrared imaging camera (FLIR T300). The time-lapse photogrammetry approach allowed for the generation of time-series 3D point clouds of the lava flows as they evolved through time. These 3D point clouds were then transformed into digital terrain models (DTMs). Using these models, we analyzed the spatial and temporal evolution of lava flow thickness with sub-centimeter resolution (Figure 1). This setup allowed for capturing of synchronous image sets, and thus, DTMs, about 7–10 s apart, limited by the power cycle of the camera triggering device. Similar approaches have been used in natural and experimental lava flow studies at a variety of scales (Dietterich et al. 2015; Farquharson et al. 2015;

Hamilton et al. 2013; James et al. 2007). Thermal infrared imaging allowed for concurrent mapping of the surface temperature field of the lava flow through time. Individual thermal infrared images were georeferenced to coincide with time-correlative DTMs (Figure 1).

We analyzed thickness and surface temperature patterns specifically during the inflation phase. For each time step, we compared the position of the planform geometric centroid of the lava lobe (herein called *lobe centroid*) to the position of greatest lava thickness, specifically the 95th percentile of thickness. Lava flow thickness changes in experimental lavas were assumed to be mostly a result of core fluid behavior and thus allowed for the interpretation of internal pressure dynamics. We assume that the spatial variability in lobe thickness creates a pressure gradient that will drive internal flow towards the flow front. The pathway of greatest pressure gradient is approximated by a vector connecting the lobe centroid and location of highest lava thickness (Figure 2).

We also compared the position of the lobe centroid to the position of highest temperature anomaly along the downslope portion of the flow margin. High temperature anomalies along the flow margin (where breakouts tend to occur) were assumed to be regions of least crustal strength because temperature and yield strength are inversely proportional for this material. This analysis produced mean vectors for each lava lobe, reported as azimuths relative to the lobe centroid, that were then compared to the azimuth representing the observed lava flow breakout location (Figure 2). The angular difference between these vectors and the actual breakout location was reported as an angular uncertainty.

Results

For each lava flow analyzed, we report the observed breakout azimuth, the predicted breakout azimuths based on thickness and thermal observations, and the angular difference between observations and predictions (Table 1). All lava flow breakout locations were predicted by either thickness or thermal observations with an average angular uncertainty of 11° ± 9°. Using thickness patterns only, six of seven lava flow breakout locations were predicted with an average angular uncertainty of 11° ± 9° and one outlier at 65° (Figure 3). Using temperature only, five of seven lava flow breakout locations were predicted with an average angular uncertainty of 10° ± 10° (thermal data were not available for two flows) (Figure 3).

Lava flow thickness and temperature patterns in these experiments were observed to be either correlated (same position) or uncorrelated (different positions). In three of five lobes, thickness patterns and temperature patterns were uncorrelated. Observed breakout azimuths for these uncorrelated cases were always nearer to the temperature anomaly (e.g. Figure 2) (Table 1). In the other two cases, where thickness patterns and temperature patterns were correlated, the observed breakout azimuth matched predictions within about 6° uncertainty (Table 1).

Discussion

Based on these experiments, lava flow thickness and surface temperature patterns appear to be critical parameters for assessing the location of flow breakout.

This agrees with the initial hypothesis that breakouts occur near zones of weakest surrounding crust and/or highest internal pressure. Below, the implications of this analysis are discussed with respect to probabilistic and deterministic mechanisms of lobe development. Additionally, we discuss a distinctive mode of lava breakout observed in experimental lava flows.

Stochastic influences on thermal anomalies

Although lava flow thickness and temperature anomalies were treated as independent variables in these analyses, observations showed that they were correlated in some cases. As previously described, in two of the five lava lobes, the position of greatest thickness and position of the high temperature anomaly were the same, within 5 – 6° angular uncertainty (Table 1). This is not surprising given that the thickest portion of a lava lobe is likely the site of highest thermal mass and can thus maintain a hotter and weaker adjoining crust. For the other three lava lobes, however, the positions of highest thickness and highest temperature were not the same (e.g., Figure 2). Thus, for these lobes, some other process influenced the crustal temperature field and therefore, the location of breakout.

These two situations represent end-member cases wherein the location of a thermal anomaly, and thus, weakest crust, is either random or correlated to lobe thickness patterns. In the random case, lava breakout location is influenced by stochastic processes involving randomly imparted crustal temperature anomalies. In the correlated case, lava breakout location is deterministic, driven by established subcrustal fluid pathways. This means that although thermal anomalies remain a good predictor for breakout location,

the origin of a thermal anomaly can depend on other stochastic processes. This observation agrees with previous studies of pāhoehoe emplacement modeling which handle breakout location with a combination of deterministic and probabilistic parameters (Glaze and Baloga 2013; Glaze and Baloga 2016; Hamilton et al. 2013).

Future experiments and observations of natural flows may help illuminate the stochastic processes influencing thermal anomalies and breakout locations. More importantly, additional observations are needed to reveal the relative frequency of random and non-random breakout locations. In this study, random breakouts (i.e. non-correlated temperature anomalies) occurred in three of five lava lobes. This suggests a strong influence of stochastic processes, but a much higher N value is needed to assess the statistical significance of this observation.

Implications for breakout mode

The hypothesis set forth in this study was based on observations of natural pāhoehoe lavas, which tend to breakout during failure of the brittle crust layer and/or hyperextension of the viscoelastic layer (Hon et al. 1994). Pāhoehoe lobe behavior observed in laboratory lavas, however, exhibited a mode of lava breakout that has not been previously described. As discussed above, breakouts in experimental lobes tended to occur due to pressure-driven uplift of the outer brittle crust and direct exposure of the weaker viscoelastic layer. Once the viscoelastic layer was exposed, a breakout occurred and was sustained, and the brittle crust remained uplifted (Figure 4). Additionally, during this process, the viscous fluid tended to wedge beneath the quartz sand layer, creating a ridge of disturbed substrate near the location of breakout (Figure

4). These observations suggest that the outer brittle crust was sufficiently strong as to resist failure, but internal fluid pressure exceeded the weight of the crust, driving uplift.

The importance of this observation is that although surface temperature appears to be a factor in determining breakout location, breakout itself is a pressure-driven process. The internal fluid pressure, however, does not exceed the yield strength of the outermost brittle crust but instead uplifts it from the substrate, thereby exposing a weaker viscoelastic layer. The apparent coincidence between breakout locations and surface temperature anomalies likely reflects a weakness at depth affecting a portion of the viscoelastic crust, which is exposed prior to breakout. In other words, when the lava lobe uplifts and exposes the viscoelastic crust (Figure 4B), the incipient breakout occurs at the weakest point of the newly exposed layer, which is coincident with the location of hottest overlying brittle crust.

This newly described mechanism illustrates that lavas can breakout with total fluid pressures lower than that required to break through the visible surface crust. Although these represent laboratory observations, similar patterns may be observed in natural lavas with similar emplacement conditions (e.g. volume-limited, moderate slope, low effusion rate). Further experiments could reveal a numerical relationship between fluid pressure and timing of breakout.

Conclusions

Breakout locations in experimental basaltic lava flows can be predicted within an angular uncertainty of about 10° by careful observations of time-series thickness and surface temperature patterns. Lava flow thickness highs represent regions of greatest

internal fluid pressure and surface temperature anomalies near the flow margin (where breakouts tend to occur) represent regions of lowest crustal strength. These results may help inform future numerical simulations of pāhoehoe lava flows. Observations of experimental lava flows also reveal a distinctive mechanism for lava breakout, wherein core fluid pressure uplifts the solid crust and allows fluid escape through the exposed, weaker, viscoelastic crust. This suggests breakouts in experimental lavas are pressure-driven, but breakouts can occur at pressures below the yield strength of the brittle surface crust.

Tables

Table 1. Table 1. Results of breakout direction prediction analysis. All values are in degrees (°)

Flow number	Azimuth	Predicted breakout (thickness)	1σ	Predicted breakout (temperature)	1σ	Angular misfit (thickness)	Angular misfit (temperature)	Angular misfit (average)	Note
171104	59	69.0	4.8	-	-	10.0	-	-	No FLIR data
180408	97	91.5	7.0	-	-	5.5	-	-	No FLIR data
180410	133	132.0	2.3	138.2	1.0	1.0	5.2	2.1	-
180414	24	46.2	12.2	16.1	0.8	22.2	7.9	7.2	-
180718-1	98	89.1	10.5	94.5	2.5	8.9	3.5	6.2	-
180719-3	38	102.6	3.6	11.0	-	64.6	27.0	18.8	-
180721-2	104	84.9	0.9	111.1	1.7	19.1	7.1	6.0	Figure 2
x	-	-	5.9	-	1.5	18.8	10.1	8.0	-
1σ	-	-	4.2	-	0.8	21.5	9.6	5.7	-

Figures

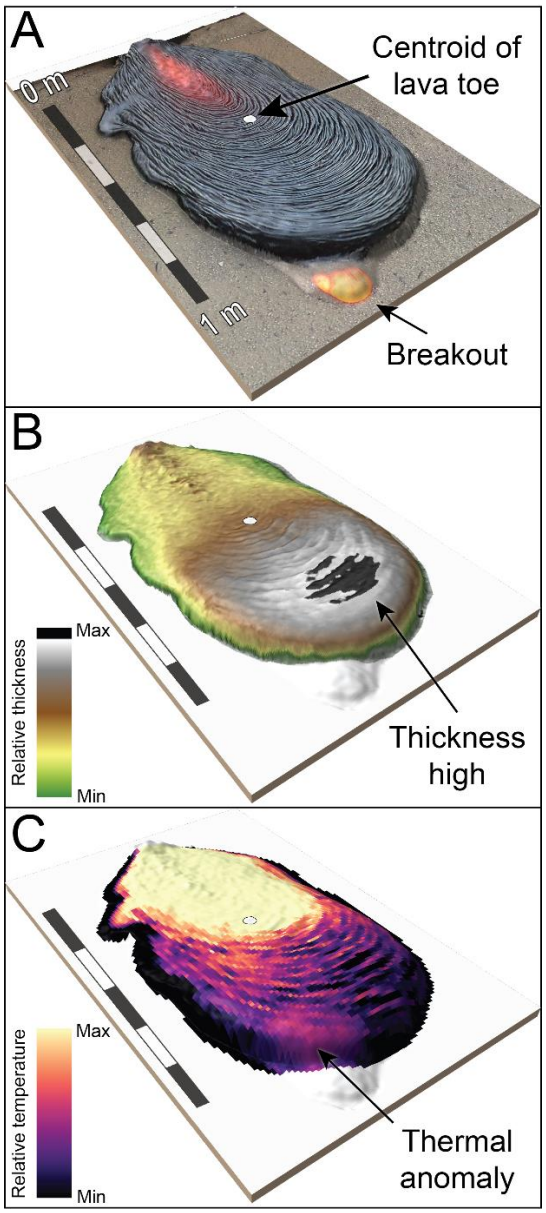

Figure 1. Experimental lava flow 180721-2 displayed as raster datasets draped over a photogrammetric 3D surface. A: Orthomosaic of inflated lava lobe, a few seconds after breakout occurs. B: Digital terrain model of inflated lava lobe – data coverage from a few seconds before breakout. C: FLIR thermal infrared image of inflated lava lobe – data coverage also from a few seconds before breakout.

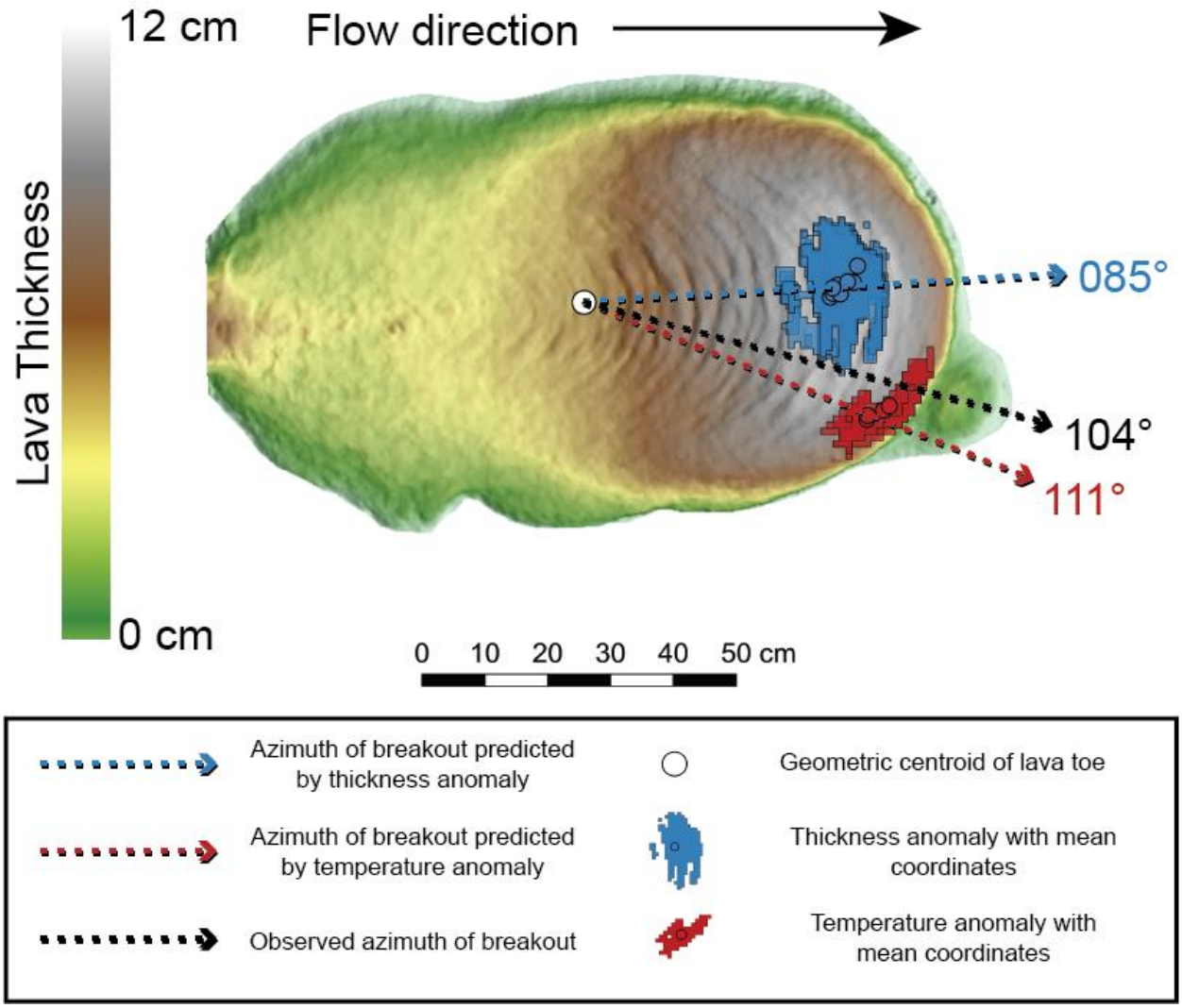

Figure 2. Predicted and observed lava flow breakout azimuths for experimental lava flow 180721-1. Base map – digital terrain model of lava flow after breakout (Figure 1B). All thickness and temperature anomaly data precede breakout.

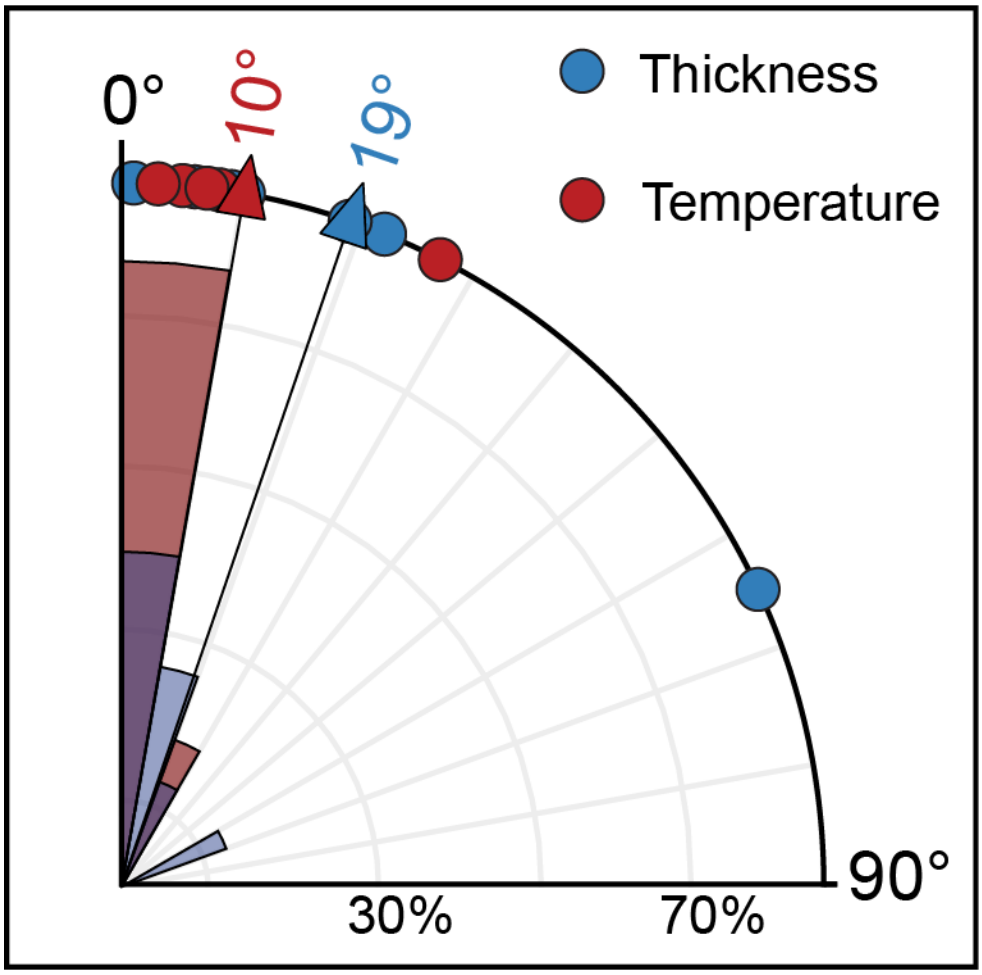

Figure 3. Rose diagram of angular misfits between predicted and observed lava flow breakout azimuths based on thickness (N = 7) and temperature (N = 5) analyses.

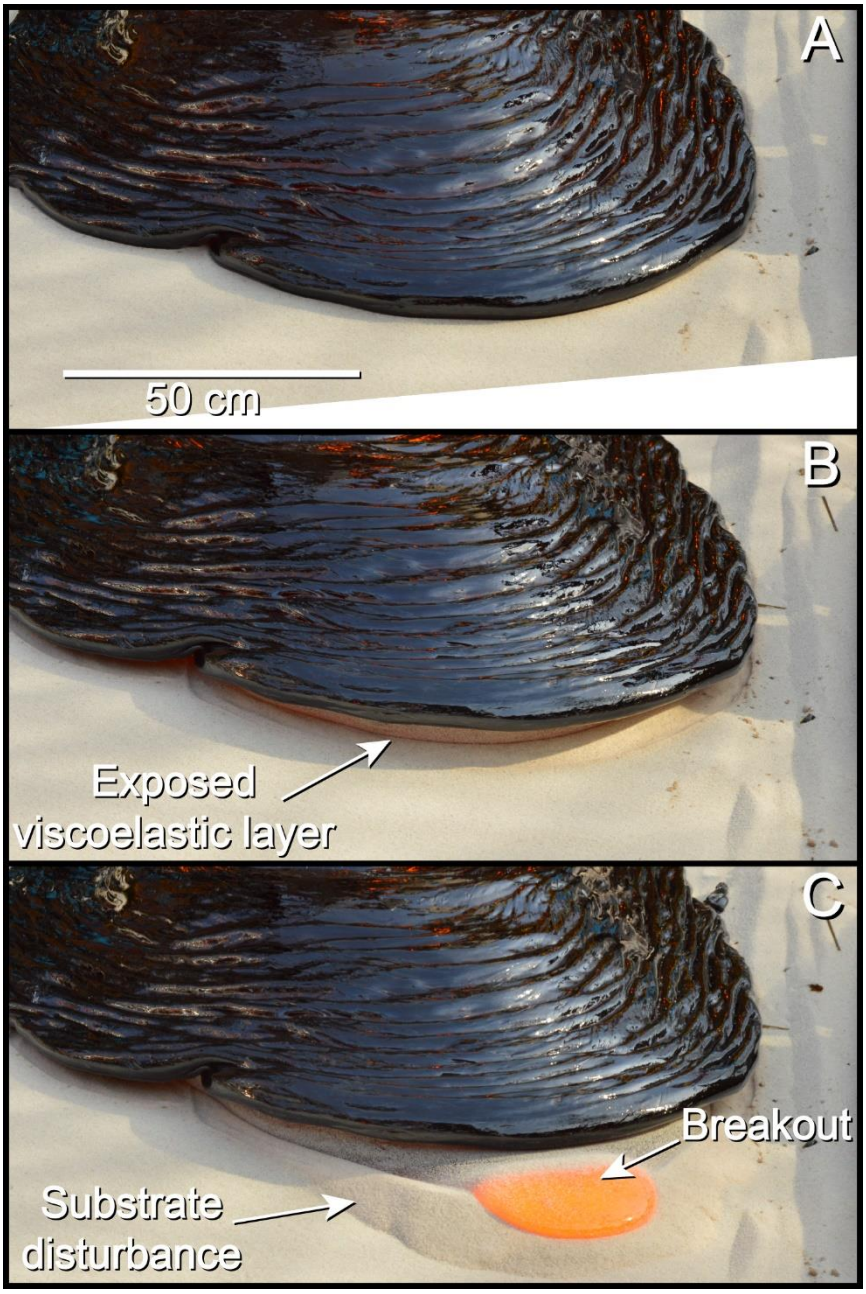

Figure 4. Time lapse oblique photographs of experimental lava lobe undergoing inflation and breakout. Total time lapse – 80 seconds. A – front of stalled lava lobe undergoing inflation. B – Inflation-driven uplift of the overlying crust exposes underlying viscoelastic crust. C – Viscous breakout occurs after breaking through exposed viscoelastic crust.

References

Anderson, S., Stofan, E., Smrekar, S., Guest, J., & Wood, B. (1999). Pulsed inflation of pahoehoe lava flows: implications for flood basalt emplacement. *Earth and Planetary Science Letters, 168*(1-2), 7-18.

Applegarth, L. J., James, M. R., Van Wyk de Vries, B., & Pinkerton, H. (2010). Influence of surface clinker on the crustal structures and dynamics of'a'ā lava flows. *Journal of Geophysical Research: Solid Earth, 115*(B7).

Baloga, S., & Glaze, L. (2003). Pahoehoe transport as a correlated random walk. *Journal of Geophysical Research: Solid Earth, 108*(B1).

Barton, M., & Huijsmans, J. P. (1986). Post-caldera dacites from the Santorini volcanic complex, Aegean Sea, Greece: an example of the eruption of lavas of near-constant composition over a 2,200 year period. *Contributions to Mineralogy and Petrology, 94*(4), 472-495.

Biot, M. A. (1961). Theory of folding of stratified visco-elastic media and its implications in tectonics and orogenesis. *Geological Society of America Bulletin, 72*, 1595-1620.

Bottinga, Y., & Weill, D. F. (1972). The viscosity of magmatic silicate liquids: a model for calculation. *American Journal of Science, 272*, 438-475.

Breard, E. C., Lube, G., Jones, J. R., Dufek, J., Cronin, S. J., Valentine, G. A., & Moebis, A. (2016). Coupling of turbulent and non-turbulent flow regimes within pyroclastic density currents. *Nature Geoscience, 9*(10), 767.

Bruno, B., Taylor, G., Rowland, S., & Baloga, S. (1994). Quantifying the effect of rheology on lava-flow margins using fractal geometry. *Bulletin of Volcanology, 56*(3), 193-206.

Byrnes, J. M., & Crown, D. A. (2001). Relationships between pahoehoe surface units, topography, and lava tubes at Mauna Ulu, Kilauea Volcano, Hawaii. *Journal of Geophysical Research, 106*, 2139-2151.

Cashman, K., Soule, S., Mackey, B., Deligne, N., Deardorff, N., & Dietterich, H. (2013). How lava flows: New insights from applications of lidar technologies to lava flow studies. *Geosphere, 9*(6), 1664-1680.

Cashman, K. V., Thornber, C., & Kauahikaua, J. P. (1999). Cooling and crystallization of lava in open channels, and the transition of Pahoehoe Lava to ʻAʻa. *Bulletin Volcanologique, 61*, 306-323.

Castro, J., & Cashman, K. V. (1999). Constraints on rheology of obsidian lavas based on mesoscopic folds. *Journal of Structural Geology, 21*, 807-819.

Chevrel, M. O., Harris, A. J., James, M. R., Calabrò, L., Gurioli, L., & Pinkerton, H. (2018). The viscosity of pāhoehoe lava: In situ syn-eruptive measurements from Kilauea, Hawaii. *Earth and Planetary Science Letters, 493*, 161-171.

Cordonnier, B., Lev, E., & Garel, F. (2016). Benchmarking lava-flow models. *Geological Society, London, Special Publications, 426*(1), 425-445.

Crown, D. A., & Baloga, S. M. (1999). Pahoehoe toe dimensions, morphology, and branching relationships at Mauna Ulu, Kilauea Volcano, Hawaiʻi. *Bulletin Volcanologique, 61*, 288-305.

Dietterich, H. R., Cashman, K. V., Rust, A. C., & Lev, E. (2015). Diverting lava flows in the lab. *Nature Geoscience, 8*(7), 494.

Dietterich, H. R., Lev, E., Chen, J., Richardson, J. A., & Cashman, K. V. (2017). Benchmarking computational fluid dynamics models of lava flow simulation for hazard assessment, forecasting, and risk management. *Journal of Applied Volcanology, 6*(1), 9.

Edwards, B. R., Karson, J. A., Wysocki, R. J., Lev, E., Binderman, I., & Kueppers, U. (2013). Insights on lava-ice/snow interactions from large-scale basaltic melt experiments. *Geology, 41*, 851-854. doi:doi:10.1130/G34305.1

Farquharson, J., James, M., & Tuffen, H. (2015). Examining rhyolite lava flow dynamics through photo-based 3D reconstructions of the 2011–2012 lava flowfield at Cordón-Caulle, Chile. *Journal of Volcanology and Geothermal Research, 304*, 336-348.

Farrell, J., Karson, J., Soldati, A., & Wysocki, R. (2018). Multiple-generation folding and non-coaxial strain of lava crusts. *Bulletin of Volcanology, 80*(12), 84.

Favalli, M., Fornaciai, A., Nannipieri, L., Harris, A., Calvari, S., & Lormand, C. (2018). UAV-based remote sensing surveys of lava flow fields: a case study from Etna's 1974 channel-fed lava flows. *Bulletin of Volcanology, 80*(3), 29.

Fink, J. (1980). Surface folding and viscosity of rhyolite flows. *Geology, 8*(5), 250-254.

Fink, J. H. (1980). Surface folding and viscosity of rhyolite flows. *Geology, 8*, 250-254.

Fink, J. H., & Fletcher, R. C. (1978). Ropy pahoehoe; surface folding of a viscous fuid. *Journal of Volcanology and Geothermal Research, 4*, 151-170.

Fink, J. H., & Griffiths, R. W. (1990). Radial spreading of viscous gravity currents with solidifying crust. *Journal of Fluid Mechanics, 221*, 485-509.

Fink, J. H., & Griffiths, R. W. (1992). A laboratory analog study of the surface morphology of lava flows extruded from point and line sources. *Journal of Volcanology and Geothermal Research, 54*, 19-32.

Fink, J. H., & Zimbelman, J. R. (1986). Rheology of the 1983 Royal Gardens basalt flows, Kilauea volcano, Hawaii. *Bulletin of Volcanology, 48*(2-3), 87-96.

Fletcher, R. C. (1974). Wavelength selection in the folding of a single layer with power-law rheology. *American Journal of Science, 274*(9), 1029-1043.

Giordano, D., & Dingwell, D. B. (2003). Non-Arrhenian multicomponent melt viscosity: a model. *Earth and Planetary Science Letters, 208*(3-4), 337-349.

Giordano, D., Polacci, M., Longo, A., Papale, P., Dingwell, D., Boschi, E., & Kasereka, M. (2007). Thermo-rheological magma control on the impact of highly fluid lava flows at Mt. Nyiragongo. *Geophysical research letters, 34*(6).

Giordano, D., Russell, J. K., & Dingwell, D. B. (2008). Viscosity of magmatic liquids: A model. *Earth and Planetary Science Letters, 271*, 123-134.

Glaze, L. S., & Baloga, S. M. (2013). Simulation of inflated pahoehoe lava flows. *Journal of Volcanology and Geothermal Research, 255*, 108-123.

Glaze, L. S., & Baloga, S. M. (2016). Simulation of cooling and pressure effects on inflated pahoehoe lava flows. *Journal of Geophysical Research: Solid Earth, 121*(1), 38-47.

Gregg, T. K. (2017). Patterns and processes: subaerial lava flow morphologies: a review. *Journal of Volcanology and Geothermal Research, 342*, 3-12.

Gregg, T. K. P., & Fink, J. H. (1995). Quantification of submarine lava-flow morphology through analog experiments. *Geology, 23*, 73-76.

Gregg, T. K. P., & Fink, J. H. (2000). A laboratory investigation into the effects of slope on lava flow morphology. *Journal of Volcanology and Geothermal Research, 96*, 145-159.

Gregg, T. K. P., Fink, J. H., & Griffiths, R. W. (1998). Formulation of multiple fold generations on lava fow surfaces: Infuence of strain rate, cooling rate, and lava composition. *Journal of Volcanology and Geothermal Research, 80*, 281292.

Griffiths, R. W. (2000). Dynamics of lava flows. *Annual Reviews of Fluid Mechanics, 32*, 477-518.

Gronvold, K. (1984). Myvatn fires 1724-1729. *Chemical composition of the lava: Reykjavik, Iceland, Nordic Volcanologicai Institute, Professional Paper, 8401*, 24.

Hallworth, M. A., Huppert, H. E., & Sparks, R. S. J. (1986). A laboratory simulation of basaltic lava flows. *Modeling Geology, 11*, 93-107.

Hamilton, C. W., Glaze, L. S., James, M. R., & Baloga, S. M. (2013). Topograpic and stochastic influences on pahoehoe lava lobe emplacement. *Bulletin of Volcanology, 75*, 756-772. doi:doi:10.1007/s00445-013-0756-8

Harris, A., Bailey, J., Calvari, S., & Dehn, J. (2005). Heat loss measured at a lava channel and its implications for down-channel cooling and rheology. *Geological Society of America Special Paper 396*, 125-146.

Harris, A., & Rowland, S. (2009). Effusion rate controls on lava flow length and the role of heat loss: a review. *Studies in volcanology: the legacy of George Walker. Special Publications of IAVCEI, 2*, 33-51.

Harris, A. J., Dehn, J., James, M. R., Hamilton, C., Herd, R., Lodato, L., & Steffke, A. (2007). Pāhoehoe flow cooling, discharge, and coverage rates from thermal image chronometry. *Geophysical research letters, 34*(19).

Harris, A. J., Flynn, L. P., Matias, O., Rose, W. I., & Cornejo, J. (2004). The evolution of an active silicic lava flow field: an ETM+ perspective. *Journal of Volcanology and Geothermal Research, 135*(1-2), 147-168.

Harris, A. J. L., Dehn, J., Patrick, M., Calvari, S., Ripepe, M., & Lodato, L. (2005). Lava effusion rates from hand-held thermal infrared imagery: an example from the June 2003 effusive activity at Stromboli. *Bulletin of Volcanology, 68*(2), 107-111.

Hoblitt, R. P., Orr, T. R., Heliker, C., Denlinger, R. P., Hon, K., & Cervelli, P. F. (2012). Inflation rates, rifts, and bands in a pāhoehoe sheet flow. *Geosphere, 8*(1), 179-195.

Hon, K., Kauahikaua, J. P., Denlinger, R., & Mackay, K. (1994). Emplacement and inflation of pahoehoe sheet flows: Observations and measurements of active lava flows on Kilauea Volcano, Hawaii. *Geological Society of America Bulletin, 106*(3), 351-370.

Horn, B. K., & Schunck, B. G. (1981). Determining optical flow. *Artificial intelligence, 17*(1-3), 185-203.

Hulme, G. (1974). The interpretation of lava flow morphology. *Geophysical Journal International, 39*(2), 361-383.

Iezzi, G., & Ventura, G. (2000). Kinematics of lava flows based on fold analysis. *Geophysical research letters, 27*(8), 1227-1230.

James, M., & Robson, S. (2012). Straightforward reconstruction of 3D surfaces and topography with a camera: Accuracy and geoscience application. *Journal of Geophysical Research: Earth Surface, 117*(F3).

James, M., & Robson, S. (2014). Sequential digital elevation models of active lava flows from ground-based stereo time-lapse imagery. *ISPRS Journal of Photogrammetry and Remote Sensing, 97*, 160-170.

James, M., & Varley, N. (2012). Identification of structural controls in an active lava dome with high resolution DEMs: Volcán de Colima, Mexico. *Geophysical research letters, 39*(22).

James, M. R., Applegarth, L. J., & Pinkerton, H. (2012). Lava channel roofing, overflows, breaches and switching: insights from the 2008–2009 eruption of Mt. Etna. *Bulletin of Volcanology, 74*(1), 107-117.

James, M. R., Pinkerton, H., & Robson, S. (2007). Image-based measurement of flux variation in distal regions of active lava flows. *Geochemistry, Geophysics, Geosystems, 8*(3).

Jeffreys, H. (1925). Lxxxiv. the flow of water in an inclined channel of rectangular section. *The London, Edinburgh, and Dublin Philosophical Magazine and Journal of Science, 49*(293), 793-807.

Kent, R. W., Thomson, B. A., Skelhorn, R. R., Kerr, A. C., Norry, M. J., & Walsh, J. N. (1998). Emplacement of Hebridean Tertiary flood basalts: evidence from an inflated pahoehoe lava flow on Mull, Scotland. *Journal of the Geological Society, 155*(4), 599-607.

Kerr, R., Griffiths, R., & Cashman, K. (2006). Formation of channelized lava flows on an unconfined slope. *Journal of Geophysical Research: Solid Earth, 111*(B10).

Kilburn, C. (1996). Patterns and predictability in the emplacement of subaerial lava flows and flow fields *Monitoring and mitigation of volcano hazards* (pp. 491-537): Springer.

Kilburn, C. R. J. (1996). Patterns and predictability in the emplacement of subaerial lava fows and flow felds. In R. Scarpa & R. I. Tilling (Eds.), *Monitoring and Mitigation of Volcano Hazards*. Berlin: Springer Verlag.

Kolzenburg, S., Jaenicke, J., Münzer, U., & Dingwell, D. (2018). The effect of inflation on the morphology-derived rheological parameters of lava flows and its implications for interpreting remote sensing data-A case study on the 2014/2015 eruption at Holuhraun, Iceland. *Journal of Volcanology and Geothermal Research, 357*, 200-212.

Lescinsky, D. T., & Merle, O. (2005). Extensional and compressional strain in lava flows and the formation of fractures in surface crust. *SPECIAL PAPERS-GEOLOGICAL SOCIETY OF AMERICA, 396*, 163.

Lescinsky, D. T., Skoblenick, S. V., & Mansinha, L. (2007). Automated identification of lava flow structures using local Fourier spectrum of digital elevation data. *Journal of Geophysical Research: Solid Earth, 112*(B5).

Lev, E., Spiegelman, M., Wysocki, R. J., & Karson, J. A. (2012). Investigating lava flow rheology using video analysis and numerical flow models. *Journal of Volcanology and Geothermal Research, 24-248*, 62-73. doi:doi.org/10.1016/j.jvolgeores.2012.08.002

Lube, G., Breard, E., Cronin, S., & Jones, J. (2015). Synthesizing large-scale pyroclastic flows: Experimental design, scaling, and first results from PELE. *Journal of Geophysical Research: Solid Earth, 120*(3), 1487-1502.

Lucas, B. D., & Kanade, T. (1981). An iterative image registration technique with an application to stereo vision.

Macdonald, G. A. (1953). Pahoehoe, aa, and block lava. *American Journal of Science, 251*, 169-191.

Magnall, N., James, M. R., Tuffen, H., & Vye-Brown, C. (2017). Emplacing a cooling-limited rhyolite lava flow: similarities with basaltic lava flows. *Frontiers in Earth Science, 5*, 44.

Marsh, B. D. (1981). On the crystallinity, probability of occurrence, and rheology of lava and magma. *Contributions to Mineralogy and Petrology, 78*, 85-98.

Merle, O. (1989). Strain models within spreading nappes. *Tectonophysics, 165*(1), 57-71.

Merle, O. (1998). Internal strain within lava flows from analogue modelling. *Journal of Volcanology and Geothermal Research, 81*(3-4), 189-206.

Murase, T., & McBirney, A. (1973). Properties of some common igneous rocks and their melts at high temperatures. *Geological Society of America Bulletin, 84*, 3563-3592.

Newhall, C., & Melson, W. (1983). Explosive activity associated with the growth of volcanic domes. *Journal of Volcanology and Geothermal Research, 17*(1-4), 111-131.

Nichols, R. L. (1939). Viscosity of lava. *the Journal of Geology, 47*(3), 290-302.

Odonne, F., & Vialon, P. (1983). Analogue models of folds above a wrench fault. *Tectonophysics, 99*(1), 31-46.

Patrick, M. R., Harris, A. J., Ripepe, M., Dehn, J., Rothery, D. A., & Calvari, S. (2007). Strombolian explosive styles and source conditions: insights from thermal (FLIR) video. *Bulletin of Volcanology, 69*(7), 769-784.

Peitersen, M. N., & Crown, D. A. (2000). Correlations between topography and intraflow width behavior in Martian and terrestrial lava flows. *Journal of Geophysical Research: Planets, 105*(E2), 4123-4134.

Program, G. V. (2004). Report on Piton de la Fournaise (France). *Bulletin of the Global Volcanism Network, 29:12*(In: Wunderman, R (ed.)).

Pyle, D. M., & Elliott, J. R. (2006). Quantitative morphology, recent evolution, and future activity of the Kameni Islands volcano, Santorini, Greece. *Geosphere, 2*(5), 253-268.

Ridley, J., & Casey, M. (1989). Numerical modeling of folding in rotational strain histories: Strain regimes expected in thrust belts and shear zones. *Geology, 17*(10), 875-878.

Rumpf, M. E., Lev, E., & Wysocki, R. (2018). The influence of topographic roughness on lava flow emplacement. *Bulletin of Volcanology, 80*(7), 63.

Sakimoto, S. E. H., & Gregg, T. K. P. (2001). Channeled flow: Analytic solutions, laboratory experiments, and applications to lava flows. *Journal of Geophysical Research, 106*, 8629-8644. doi:doi:10.1029/2000JB900384

Sehlke, A., & Whittington, A. G. (2016). The viscosity of planetary tholeiitic melts: A configurational entropy model. *Geochimica et Cosmochimica Acta, 191*, 277-299.

Self, S., Keszthelyi, L., & Thordarson, T. (1998). The importance of pahoehoe. *Annual Reviews of Earth and Planetary Science, 26*, 81-110.

Self, S., Thordarson, T., & Keszthelyi, L. (1997). Emplacement of continental flood basalt lava flows *Large Igneous Provinces: Continental, Oceanic, and Planetary Flood Volcanism* (Vol. Geophysical Monograph 100, pp. 381-410). Washington, DC: American Geophysical Union.

Shaw, H. R. (1972). Viscosities of magmatic silicate liquids: An empirical method of prediction

American Journal of Science, 272, 870-893.

Slatcher, N., James, M. R., Calvari, S., Ganci, G., & Browning, J. (2015). Quantifying effusion rates at active volcanoes through integrated time-lapse laser scanning and photography. *Remote Sensing, 7*(11), 14967-14987.

Sparks, R. S. J. (1997). Causes and consequences of pressurisation in lava dome eruptions. *Earth and Planetary Science Letters, 150*(3-4), 177-189.

Sparks, R. S. J., Pinkerton, H., & Hulme, G. (1976). Classification and formation of lava levees on Mount Etna, Sicily. *Geology, 4*, 269-271.

Staudacher, T., Ruzié, L., & Peltier, A. (2008). Historique des éruptions du Piton de la Fournaise de 1998 à 2007. *Graphica (St Denis, La Réunion), 97*.

Tedesco, D., Vaselli, O., Papale, P., Carn, S., Voltaggio, M., Sawyer, G., . . . Tassi, F. (2007). January 2002 volcano-tectonic eruption of Nyiragongo volcano, Democratic Republic of Congo. *Journal of Geophysical Research: Solid Earth, 112*(B9).

Theilig, E., & Greeley, R. (1986). Lava flows on Mars: Analysis of small surface features and comparisons with terrestrial analogs. *Journal of Geophysical Research: Solid Earth, 91*(B13).

Thielicke, W., & Stamhuis, E. J. (2014). PIVlab-towards user-friendly, affordable and accurate digital particle image velocimetry in MATLAB. *Journal of Open Research Software, 2*.

Thordarson, T. D., & Self, S. (1998). The Roza member, Columbia River Basalt group: A gigantic pahoehoe lava flow field formed by endogenous processes? . *Journal of Geophysical Research, 103*, 27411–27445.

Vlastélic, I., Peltier, A., & Staudacher, T. (2007). Short-term (1998–2006) fluctuations of Pb isotopes at Piton de la Fournaise volcano (Réunion Island): origins and constraints on the size and shape of the magma reservoir. *Chemical Geology, 244*(1), 202-220.

Vye-Brown, C., Self, S., & Barry, T. (2013). Architecture and emplacement of flood basalt flow fields: case studies from the Columbia River Basalt Group, NW USA. *Bulletin of Volcanology, 75*(3), 697.

Walker, G. (2009). The endogenous growth of pahoehoe lava lobes and morphology of lava-rise edges. *Studies in volcanology—the legacy of George Walker (Special Publications of IAVCEI No. 2). The Geol Soc*, 17-32.

Walker, G. P. (1991). Structure, and origin by injection of lava under surface crust, of tumuli,“lava rises”,“lava-rise pits”, and “lava-inflation clefts” in Hawaii. *Bulletin of Volcanology, 53*(7), 546-558.

Walter, T. R. (2011). Low cost volcano deformation monitoring: optical strain measurement and application to Mount St. Helens data. *Geophysical Journal International, 186*(2), 699-705.

Warner, N. H., & Gregg, T. K. (2003). Evolved lavas on Mars? Observations from southwest Arsia Mons and Sabancaya volcano, Peru. *Journal of Geophysical Research: Planets, 108*(E10).

Webb, S. L., & Dingwell, D. B. (1990). Non-Newtonian rheology of igneous melts at high stresses and strain rates: Experimental results for rhyolite, andesite, basalt, and nephelinite. *Journal of Geophysical Research: Solid Earth, 95*(B10), 15695-15701.

Welch, P. (1967). The use of fast Fourier transform for the estimation of power spectra: a method based on time averaging over short, modified periodograms. *IEEE Transactions on audio and electroacoustics, 15*(2), 70-73.

Westoby, M., Brasington, J., Glasser, N., Hambrey, M., & Reynolds, J. (2012). 'Structure-from-Motion'photogrammetry: A low-cost, effective tool for geoscience applications. *Geomorphology, 179*, 300-314.

Wirth, K. R., Naiman, Z. J., & Vervoort, J. D. (1997). The Chengwatana Volcanics, Wisconsin and Minnesota: petrogenesis of the southernmost volcanic rocks exposed in the Midcontinent rift. *Canadian Journal of Earth Sciences, 34*(4), 536-548.

Wright, R., Flynn, L. P., Garbeil, H., Harris, A. J., & Pilger, E. (2004). MODVOLC: near-real-time thermal monitoring of global volcanism. *Journal of Volcanology and Geothermal Research, 135*(1-2), 29-49.

Zimbelman, J. R. (1985). Estimates of rheologic properties for flows on the Martian volcano Ascraeus Mons. *Journal of Geophysical Research: Solid Earth, 90*(S01), 157-162.

Biographical Data

Name of Author: James Arnold Farrell

Place of Birth: Syracuse, New York

Date of Birth: August 5, 1990

Graduate and Undergraduate Schools Attended:

Stony Brook University, Stony Brook, NY

University of Connecticut, Storrs, CT

Degrees Awarded:

Master of Science, 2015, University of Connecticut

Bachelor of Science, 2012, Stony Brook University

Awards and Honors:

Newton E. Chute Award

Vincent E McKelvey scholarship

Outstanding Graduate Research Award – UConn Geosciences

Outstanding Graduate Poster Award – Northeast GSA

GeoPRISMS Student Presentation Award (honorable mention)

Professional Experience:

Teaching assistant. Department of Earth Sciences, Syracuse University, Syracuse, NY. 2016-2019.

Research assistant. Department of Earth Sciences, Syracuse University, Syracuse, NY. 2016.

Teaching assistant. Center for Integrative Geosciences, University of Connecticut, Storrs, CT. 2013-2015.

Publications:

Farrell J, Karson J, Soldati A, Wysocki R. 2018. Multiple-generation folding and non-coaxial strain of lava crusts. Bulletin of Volcanology. https://doi.org/10.1007/s00445-018-1258-5.

Karson J, Farrell J, Chutas L, Nanfito A, Proett J, Runnals K, Sæmundsson K. 2018. Rift-parallel strike-slip faulting near the Iceland plate boundary zone: Implications for propagating rifts.Tectonics. https://doi.org/10.1029/2018TC005206.

Karson J, Brandsdottir B, Einarsson P, Saemundsson K, Farrell J, Horst A. Evolution of migrating transform faults in anisotropic oceanic crust-examples from Iceland. CJES. http://dx.doi.org/10.1139/cjes-2018-0260.